Original Article

The aging-induced long non-coding RNA *MIRIAL* controls endothelial cell and mitochondrial function

Short title: The lncRNA *MIRIAL* in endothelial cells

Caroline Kohnle [1,2], Susanne Koziarek [1], Timothy Warwick [2,3], Kosta Theodorou [1], Ariane Fischer [1], Rio Putra Juni [5], Marion Muhly-Reinholz [1], Denise Busscher [1], Frederike Lam [2,3], Felix Vetter [1], Julian U. G. Wagner [1,2,4], Janina Sommer [1], Anna Theresa Gimbel [1,2], Laura Stanicek [1,5], Stefan Günther [2,4,6], Ilka Wittig [7], Lars Maegdefessel [8,9,10], Matthias S. Leisegang [2,3], Ralf P. Brandes [2,3,4], Stefanie Dimmeler [1,2,4], Reinier A. Boon [1,2,4,5,†]

Affiliations:

[1]Goethe University Frankfurt, Faculty of Medicine, Centre of Molecular Medicine, Institute of Cardiovascular Regeneration, Frankfurt am Main, Germany.
[2]German Centre for Cardiovascular Research DZHK, Partner Site Rhine-Main, Berlin, Germany.
[3]Goethe University Frankfurt, Faculty of Medicine, Institute for Cardiovascular Physiology, Frankfurt am Main, Germany.
[4]Cardiopulmonary Institute (CPI), 60590 Frankfurt am Main, Germany.
[5]Department of Physiology, Amsterdam Cardiovascular Science, VU University Medical Centre, Amsterdam, The Netherlands.
[6]Max Planck Institute for Heart and Lung Research, Bad Nauheim, Germany.
[7]Goethe University Frankfurt, Faculty of Medicine, Functional Proteomics, Frankfurt am Main, Germany.
[8]Department of Vascular and Endovascular Surgery, Technical University Munich, Munich, Germany.
[9]German Centre for Cardiovascular Research DZHK, Partner Site Munich, Berlin, Germany.
[10]Department of Medicine, Karolinska Institute, Stockholm, Sweden.

† Corresponding author: Reinier A. Boon, boon@med.uni-frankfurt.de, Theodor-Stern-Kai 7 60590 Frankfurt am Main, Germany

Total word count: 9,475

Abstract

Aims: Vascular aging is characterized by the progressive deterioration of endothelial function. Long non-coding RNAs (lncRNAs) are critical regulators of gene expression and protein function. However, their involvement in aging-related dysregulation of endothelial cell function remains largely unknown. Here, we aim to characterize the aging-regulated lncRNA *MIRIAL* in endothelial cells.

Methods + Results: We identified *Mirial* as an aging-induced lncRNA in RNA-sequencing data of mouse cardiac endothelial cells. In human umbilical vein endothelial cells (HUVECs), gapmer-mediated knockdown of *MIRIAL* led to decreases in proliferation, migration and basal angiogenic sprouting. Additionally, *MIRIAL* knockdown led to increased mitochondrial mass, spare respiratory capacity, and vascular endothelial growth factor (VEGF)-stimulated sprouting. Mechanistically, we demonstrate that *MIRIAL* forms an *RNA*·DNA:DNA triple helix (triplex) with a regulatory region of the quiescence-promoting Forkhead Box O1 (*FOXO1*) gene, thus inducing its expression. The formation of this triplex involves an *Alu* element within the *MIRIAL* transcript, representing a previously undescribed mechanism of action for a lncRNA. Further, we generated a global *Mirial* knockout mouse line of. Angiogenic sprouting of aortic rings from *Mirial* knockout mice was reduced under basal conditions, but increased after VEGF administration, validating the *in vitro* angiogenic phenotype. Importantly, cardiac contractile function after acute myocardial infarction is severely reduced in *Mirial* knockout mice, as compared to wild-type littermates.

Conclusions: The lncRNA *MIRIAL* is an aging-induced regulator of endothelial quiescence and metabolism.

Key words: Long non-coding RNAs; endothelial cells; aging; quiescence; triple helix

55 **Translational Perspective**

56 LncRNAs often exhibit cell-type or tissue-specific expression and regulation, rendering them
57 potentially druggable targets requiring lower doses and having fewer side effects compared
58 to protein targets. Our current research highlights, that loss of *Mirial* correlates with
59 adverse outcomes post-acute myocardial infarction in a murine model. Dysregulation of
60 *MIRIAL* in various human pathological conditions, such as ischemic heart disease, abdominal
61 aortic aneurysm, cancer, and aging, indicates its potential as a diagnostic marker.
62 Mechanistically, *MIRIAL* regulates endothelial quiescence by modulating *FOXO1* expression,
63 suggesting it as a promising therapeutic target to counteract the age-related decline in
64 endothelial cell function.

65 **1. Introduction**

66 LncRNAs are a heterogeneous class of RNA defined by a length exceeding 200 nucleotides
67 and often exhibit a low abundance per cell. They can interact with DNA, other RNAs or
68 proteins, thereby regulating gene expression, as well as RNA and protein function[1, 2].
69 Cardiovascular diseases (CVD) remain the leading cause of mortality worldwide[3]. The
70 predominant risk factor for the development of CVD is aging[4]. In the vasculature, aging
71 manifests as a gradual decline of endothelial function, stiffening of the vessel wall,
72 compromised angiogenic capacity and chronic inflammation[5]. The transcription factor
73 FOXO1 promotes endothelial quiescence and is indispensable for endothelial cell
74 homeostasis, vasculogenesis, and development[6, 7].

75 We identified an aging-induced lncRNA in murine cardiac endothelial cells that we termed
76 *Mirial* (**Mi**cro**R**NA-cluster 23a~27a~24-2-associated and **I**nduced by **A**ging **L**ong non-coding
77 RNA) (transcript ID: Gm26532, ENSMUSG00000097296), which is previously uncharacterized
78 in endothelial cells. Prior publications have linked lower *Mirial* expression to reduced FoxO
79 signaling in mice[8]. In humans, upregulation of the orthologous lncRNA *MIRIAL* (transcript
80 IDs: LOC284454, AL832183, MIR23AHG, ENSG00000267519 or AC020916.1) was reported in
81 nasopharyngeal carcinoma[9] and hepatocellular carcinoma[10], and was associated with
82 elevated migration and invasion and poorer clinical prognosis. Furthermore, copy number
83 variations of *MIRIAL* in colorectal carcinoma patient samples were described[11]. A study by
84 Das *et al.* revealed that *MIRIAL* is a polyadenylated, single-exonic lncRNA with a half-life of 3
85 hours that is associated with chromatin. In contrast to the aforementioned studies of
86 *MIRIAL* in cancer, they proposed its expression to be reduced in various types of cancers and
87 cancer cell lines[12]. Lastly, *MIRIAL* was demonstrated to be upregulated and may serve as
88 diagnostic biomarker in head and neck cancers[13].

89 Here, we present a comprehensive characterization of the aging-induced lncRNA *MIRIAL* in
90 endothelial cells, where it regulates metabolism and mitochondrial copy number by
91 activating FOXO1 signaling. FOXO1 represses MYC signaling and promotes endothelial
92 quiescence. Concurrent suppression of the p53 signaling pathway leads to enhanced
93 proliferation and angiogenesis. Mechanistically, we discovered that an *Alu* element within
94 the *MIRIAL* transcript forms an *RNA*·DNA:DNA triplex with a regulatory region of the *FOXO1*
95 gene, resulting in its increased expression. Importantly, *MIRIAL* is the first lncRNA harboring
96 a triplex-forming *Alu* element. Lastly, we generated a *Mirial* knockout mouse line, which
97 presents with a sensitization of endothelial cells towards VEGF-A signaling in *ex vivo*
98 experiments and a reduced myocardial contractile function after acute myocardial infarction
99 (AMI) *in vivo*.

100 ## 2. Materials and Methods

101 ### 2.1. Animals

102 All mice experiments were carried out in accordance with the principles of laboratory
103 animal care as well as according to the German national laws and the guidelines from
104 Directive 2010/63/EU of the European Parliament on the protection of animals used for
105 scientific purposes. The studies have been approved by the local ethics committee
106 (Regierungspräsidium Darmstadt, Hesse, Germany). Mice were kept in individually
107 ventilated cages (Tecniplast) at 12:12h-light/dark cycles at 21–24°C and 45-60% humidity.
108 Water and ssniff R/M-H complete feed (ssniff Spezialdiäten) were fed *ad libitum*. Young (12
109 weeks) and aged (72 weeks) wild type C57Bl/6 mice were purchased from Janvier. The
110 *MIRIAL* knockout mouse line was produced on a C57Bl/6N background by Cyagen/Taconic
111 using CRISPR/Cas9. Both, male and female animals were used for the experiments. Animals
112 were sacrificed by cervical dislocation under isoflurane (AbbVie) inhalation anesthesia. After
113 perfusion with HBSS (Gibco), organs and tissues harvested for RNA or DNA isolation were
114 snap-frozen in liquid nitrogen and homogenized in QIAzol lysis reagent (QIAGEN) or genomic
115 lysis buffer (Invitrogen), respectively, using the Bead Mill MAX Homogeniser (VWR). The
116 steps of RNA and genomic DNA isolation can be found elsewhere in this manuscript. AMI
117 surgery was performed on 11–13-week-old animals by ligation of the left anterior
118 descending (LAD) coronary artery as described before[14]. Inhalation anesthesia was induced
119 using isoflurane (Abbvie). Analgesia was conducted using buprenorphine (0.1 mg/kg) injection
120 and bupivacaine (0.25%, 1 mg/kg) infiltration. Post-operatively, buprenorphine (0.1 mg/kg) was
121 injected twice a day for two days, and carprofen (5 mg/kg) once a day for six days. The animals'
122 health status was assessed daily. Four weeks after AMI surgery, mice were euthanized and
123 perfused as described earlier and the hearts were harvested.

124 **2.2. Cell culture**

125 Pooled HUVECs were purchased from Lonza and cultured in Endothelial Cell Basal Medium
126 (EBM) (Lonza) containing EGM SingleQuots supplements (Lonza) (without ascorbic acid) and
127 10% fetal bovine serum (FBS) (Gibco). HUVECs were used at passage 2 – 3 for experiments
128 and cell number was determined using the Nucleocounter NC-2000 (Chemometec A/S).
129 Human embryonic kidney (HEK) cell lines (Lenti-X 293T) (Takara) were cultured in high-
130 glucose DMEM (Gibco) with 10 % FBS (Gibco) and 1x Pen/Strep (Roche). Lenti-X 293T cells
131 were kindly provided by the lab of Ralf Brandes/Matthias Leisegang. All cells were regularly
132 tested for mycoplasma contamination and kept at 37°C and 5% CO_2 in a humidified
133 atmosphere.

134 **2.3. Human samples**

135 Participants gave informed written consent prior to the inclusion in the study. The
136 investigation conformed to the Declaration of Helsinki. Left ventricular tissue samples from
137 ischemic heart disease (ISHD) patients and control samples were sourced from the
138 University of Sydney (Sydney, NSW, Australia) with approval from the Human Research
139 Ethics Committee (number 2012/2814). Control samples were obtained from explanted
140 hearts of heathy donors who died from non-cardiac causes, typically motor vehicle
141 accidents.

142 **2.4. RNA-sequencing**

143 HUVECs were transfected with either LNA Control or LNA MIRIAL. 48 h post-transfection,
144 RNA was isolated as described earlier. RNA quality control, library preparation, RNA-
145 sequencing and analysis was performed as described in[15]. The related data are available on

146 Gene Expression Omnibus (accession number GSE248795; reviewer token: cxutusselbenlkp;
147 https://www.ncbi.nlm.nih.gov/geo/query/acc.cgi?acc=GSE248795). Single-cell RNA-
148 sequencing data of human aneurysmal abdominal aortas was obtained from Gene
149 Expression Omnibus (accession number GSE237230)[16]. RNA-sequencing data of cardiac
150 endothelial cells derived from young and aged mice was published previously and is
151 available online[17].

152 **2.5. Statistics**

153 Statistical analysis was performed using GraphPad Prism 7.02, 8.0.1 or 9.0.2 for Windows
154 (GraphPad Software, www.graphpad.com). Results are presented as mean ± standard
155 deviation (SD) or standard error of the mean (SEM). Gaussian distribution was assessed
156 using the Shapiro-Wilk normality test. To compare two conditions, paired or unpaired
157 student's *t* test, Mann-Whitney test or Kolmogorov-Smirnov tests were used. To compare
158 multiple conditions, we used (Brown-Forsythe and Welch) analysis of variance (ANOVA) or
159 Kruskal-Wallis test with Tukey *post-hoc* test.

160 **3. Results**

161 **3.1. *MIRIAL* is an aging-induced long non-coding RNA that regulates endothelial cell**

162 **quiescence**

163 *Mirial* (transcript ID: Gm26532) was first identified in an RNA-sequencing data set generated
164 from cardiac endothelial cells of 12 weeks old and 20 months old mice **(Fig. 1A)**[17]. These
165 data showed that *Mirial* was upregulated during aging, which was further confirmed in
166 aortic intima samples of young (12 weeks) and aged (20 months) mice analyzed by qRT-PCR
167 **(Fig. 1B)**. The *Mirial* gene locus also encompasses the miRNA cluster 23a~27a~24-2 and is
168 highly conserved. By analyzing the corresponding locus in humans, the human orthologue of
169 *Mirial* could be identified **(Supp. Fig. 1A)**. Interestingly, *MIRIAL* was also found to be
170 upregulated in an RNA-sequencing data set of human native endothelial cells from young
171 and aged individuals[18]. Previously, it had been shown that *MIRIAL* is highly sequence
172 conserved solely in primates[12]. To assess the degree of sequence conservation between
173 human and mouse we employed the LALIGN DNA:DNA tool[19], which revealed that around
174 50% of the mouse sequence is also present in the human orthologue **(Supp. Fig. 1B)**.
175 Comparing the coding probability of *MIRIAL* with known transcripts using the Coding-
176 Potential Assessment Tool (CPAT)[20] we found that *MIRIAL* exhibited a coding probability
177 similar to well-known lncRNAs such as *XIST* and *MALAT1*. Conversely, protein-coding
178 transcripts like *GAPDH*, but also *ZSWIM4*, the protein-coding gene upstream in the locus of
179 *MIRIAL*, were found on the opposite side of the spectrum **(Supp. Fig. 1C)**. By performing
180 RNA-sequencing analyses, we assessed the transcription levels of *MIRIAL* in various human
181 cell types of cardiovascular origin. The results demonstrated that *MIRIAL* is expressed in
182 endothelial cells of different vascular beds, as well as in other non-endothelial cell types
183 including cardiomyocytes **(Supp. Fig. 1D)**. In the context of CVDs, *MIRIAL* expression was

184 induced in left ventricular tissue samples from patients with ischemic heart disease (ISHD)
185 **(Fig. 1C)** and in endothelial cells from human abdominal aortic aneurysm (AAA) samples
186 using single-cell RNA-sequencing **(Supp. Fig. 1E)**[16]. To investigate the function of *MIRIAL*, we
187 chose a loss-of-function approach using LNA gapmers in human umbilical vein endothelial
188 cells (HUVECs), achieving a knockdown efficiency of approximately 80-88% **(Supp. Fig. 2A)**.
189 *MIRIAL* silencing resulted in a decrease in proliferation **(Fig. 1D)** with a block of the cell cycle
190 at the G0/G1 phase **(Fig. 1E)**. A scratch-wound assay combined with electric cell-substrate
191 impedance sensing (ECIS) showed reduced barrier function **(Supp. Fig. 2B)** and impaired
192 migration **(Fig. 1F)** after *MIRIAL* knockdown. Next, we assessed whether these effects were
193 due to quiescence (a reversible reduction in cellular activity), senescence or apoptosis (both
194 of which are irreversible). Apoptosis was unchanged in *MIRIAL* knockdown cells, as assessed
195 by Caspase-3/-7 activity measurement **(Fig. 1G)**. In addition, there was no change in number
196 of senescent cells after *MIRIAL* knockdown using a senescence-associated β-galactosidase
197 staining **(Supp. Fig. 2C)**, DNA-damage-associated γ-H2A.X staining **(Supp. Fig. 2D)** or
198 telomere length measured by qPCR **(Supp. Fig. 2E)**. These results suggested that loss of
199 *MIRIAL* induces quiescence rather than senescence or apoptosis. Given the observed
200 decrease in proliferation and migration, we hypothesized that angiogenic sprouting would
201 also be reduced. This was confirmed using a spheroid sprouting assay under unstimulated
202 conditions. Importantly, stimulation with VEGF-A resulted in an increase in angiogenic
203 sprouting when *MIRIAL* was silenced, as compared to VEGF-A stimulated control cells **(Fig.**
204 **1H)**. Moreover, VEGF-A stimulation rescued the effects of *MIRIAL* knockdown on
205 proliferation **(Supp. Fig. 2F)**. Taken together, these results suggest that loss of *MIRIAL*
206 induces a reversible state of quiescence of endothelial cells.

207 **3.2. *MIRIAL* regulates endothelial mitochondrial metabolism**

208 Glycolysis serves as the predominant pathway for energy production in endothelial cells and
209 plays a central role in endothelial quiescence[21]. To investigate the potential impact of
210 *MIRIAL* on energy homeostasis in endothelial cells, we used the Seahorse glycolysis stress
211 test. Surprisingly, *MIRIAL* knockdown did not affect glycolysis **(Supp. Fig. 3A and 3B)**.
212 However, using the mitochondrial stress test, we found that *MIRIAL* knockdown led to an
213 increase in maximal respiration **(Fig. 2A and 2B)** and spare respiratory capacity (SRC) **(Fig.
214 2C)**, while basal respiration remained unchanged **(Fig. 2A and 2B)**. Furthermore, ATP
215 production **(Fig. 2D)** and cellular ATP levels were increased **(Fig. 2E)** after *MIRIAL*
216 knockdown. To determine the underlying cause of this apparent increase in mitochondrial
217 activity, we analyzed mitochondrial content after knockdown of *MIRIAL*. We found an
218 increase in mitochondrial mass **(Fig. 2F)** and mitochondrial DNA content **(Fig. 2G)** relative to
219 nuclear DNA following *MIRIAL* knockdown. Nevertheless, mitochondrial membrane
220 potential **(Supp. Fig. 3C)** and production of reactive oxygen species (ROS) **(Supp. Fig. 3D)**
221 remained unchanged, suggesting that *MIRIAL* silencing induces the number of functional
222 mitochondria.

223 The tightly regulated processes of fission and fusion play pivotal roles in maintaining the
224 cellular oxidative capacity, energy supply and biomass supply through coordinating
225 mitochondrial copy number[22]. Accordingly, we wanted to explore whether these processes
226 are involved in the mechanism by which *MIRIAL* knockdown augments mitochondrial copy
227 number. Consistent with the increase of total mitochondrial mass and mitochondrial DNA
228 content after knockdown of *MIRIAL*, we also found an elevation in the expression levels of
229 almost all key players relevant for fission and fusion, including mitochondrial fission factor
230 (MFF), dynamin 1-like protein (DRP1), Mitofusin-1, Mitofusin-2, mitochondrial dynamin like
231 GTPase Optic Atrophy 1 (OPA1) **(Supp. Fig. 4 A-G)** and the transporter of the outer

232 mitochondrial membrane (TOMM20) **(Supp. Fig. 4H)**, responsible for mitochondrial
233 membrane transport. To investigate the impact of increased levels of fission and fusion
234 proteins on mitochondrial morphology following *MIRIAL* knockdown, we utilized TOMM20
235 staining followed by immunofluorescence microscopy **(Fig. 2H)**. We quantified the
236 mitochondrial fragmentation count (MFC), aspect ratio (a measure of mitochondrial length
237 and structural integrity), and form factor (a combined measure of mitochondrial elongation
238 and branching). Our results showed a significant increase in the fragmentation count **(Fig.
239 2I)** and a reduction in the form factor **(Fig. 2J)** upon *MIRIAL* knockdown. However, the
240 aspect ratio remained unchanged **(Fig. 2K)**. These findings suggest that the loss of *MIRIAL*
241 increases mitochondrial content and function, but this effect does not seem to be mediated
242 through changes in fission or fusion. The increased fragmentation count observed after
243 *MIRIAL* silencing indicates a higher number of mitochondria. These mitochondria exhibit less
244 branching, yet their individual structural integrity and length remain unaltered. In summary,
245 these results show that knockdown of *MIRIAL* heightens functional mitochondrial content in
246 endothelial cells.

247 **3.3. *MIRIAL* knockdown in HUVECs activates the p53 signaling pathway**

248 To gain insight into the role of *MIRIAL* in endothelial cell quiescence, we first focused on its
249 subcellular localization. Subcellular fractionation of HUVECs into cytoplasmic, nucleoplasmic
250 and chromatin fractions revealed that *MIRIAL* was predominantly present in the nucleus
251 (~80%), with a significant proportion present in the chromatin fraction **(Supp. Fig. 4I)**. Given
252 this localization pattern, we hypothesized that *MIRIAL* might directly regulate gene
253 expression. To assess its impact on gene expression we performed RNA-sequencing of
254 HUVECs after *MIRIAL* knockdown, comparing them to control-transfected cells. Following

255 *MIRIAL* knockdown, 974 genes were differentially expressed (Adjusted *p*-value < 0.01,
256 absolute $\log_2$(fold change) > 0.585) **(Fig. 3A)**. Kyoto Encyclopedia of Genes and Genomes
257 (KEGG) pathway enrichment analysis demonstrated that genes associated with the cell cycle
258 were downregulated significantly **(Fig. 3B)**, aligning with our previous findings on cell
259 proliferation **(Fig. 1C)**. In addition, we observed a significant upregulation in genes
260 annotated as members of the p53 signaling pathway **(Fig. 3B)**.

261 Under basal conditions, p53 is constantly expressed and subsequently poly-ubiquitinylated
262 by the E3 ubiquitin-protein ligase MDM2, leading to its proteasomal degradation. However,
263 in response to various stressors, such as metabolic or oxidative stress, p53 undergoes
264 phosphorylation at multiple sites, resulting in its stabilization and nuclear translocation. In
265 the nucleus, p53 acts as a transcription factor regulating gene expression[23]. We validated
266 the activation of p53 target genes using qRT-PCR, showing that *MIRIAL* knockdown indeed
267 induces expression of typical p53 target genes (*HMOX1*, *LIF*, *CYFIP2*, *CMBL*, *GDF15*, *CDKN1A*,
268 and *RRM2B*). Importantly, the upregulation of p53 target genes was fully dependent on the
269 presence of p53, since knockdown of p53 using siRNA, rescued the loss-of-*MIRIAL*-mediated
270 induction of these target genes **(Fig. 3C)**. In addition, we confirmed the upregulation of p21
271 (*CDKN1A*) **(Fig. 3D)**, p53 **(Fig. 3E)** and phosphorylation of p53 at Ser15 **(Fig. 3F)** on the
272 protein level and discovered a physical interaction between p53 and *MIRIAL* using
273 crosslinking and RNA immunoprecipitation (CLIP) **(Fig. 3G)**. Interestingly, the increase in
274 mitochondrial DNA in *MIRIAL* knockdown cells could not be rescued by a simultaneous
275 knockdown of p53 **(Fig. 3H)**, indicating that p53 induction is not responsible for the
276 observed increase in mitochondrial activity following *MIRIAL* silencing.

277 The primary transcript of the *MIRIAL* locus which contains both the miRNAs and *MIRIAL* is
278 immediately cleaved by Drosha after transcription[12]. Given the mutual transcription of the
279 miRNAs and *MIRIAL*, it was essential to investigate whether a potential decrease in miRNA
280 abundance contributed to the phenotype. Using TaqMan miRNA assay probes, we assessed
281 the expression levels of all three members of the miRNA cluster (miR-23a, miR-27a and miR-
282 24-2) after *MIRIAL* knockdown. All three miRNAs were downregulated following *MIRIAL*
283 knockdown **(Supp. Fig. 5A)**. If this reduction were functionally relevant, we would expect an
284 upregulation of the target genes regulated by these miRNAs. However, expression levels of
285 two selected target genes of each miRNA did not increase after *MIRIAL* knockdown **(Supp.**
286 **Fig. 5B)**, suggesting that the moderate reduction in miRNA expression did not result in
287 target de-repression. Nonetheless, to exclude the possibility that the observed phenotype
288 resulting from silencing of *MIRIAL* is due to reduction of these miRNAs, we performed
289 miRNA overexpression experiments by transfecting HUVECs with combined pre-miRNAs
290 achieving expression levels 40-150-fold higher than control **(Supp. Fig. 5C)**. Notably, *MIRIAL*
291 knockdown efficiency was not affected by miRNA overexpression **(Supp. Fig. 5D)**. We
292 further assessed whether miRNA overexpression could rescue the functional effects of
293 *MIRIAL* knockdown on cell proliferation, mitochondrial DNA content and p53 target gene
294 expression. While miRNA overexpression increased proliferation, this effect was
295 independent of *MIRIAL*, as knockdown of *MIRIAL* still significantly decreased cell numbers
296 **(Supp. Fig. 5E)**. Additionally, mitochondrial DNA content remained elevated after *MIRIAL*
297 knockdown, despite overexpression of the miRNAs **(Supp. Fig. 5F)**. Regarding p53 target
298 gene expression, we observed that *HMOX1*, *RRM2B* and *MDM2* were the only genes
299 influenced by miRNA overexpression, with *HMOX1* being a known target of miR-24[24] **(Supp.**
300 **Fig. 5G)**. These findings strongly suggest that the effects of *MIRIAL* silencing on endothelial

301 cells are unlikely to be solely attributed to a reduction in miR-23a, miR-27a and miR-24-2
302 expression.

303 In conclusion, the results from these loss-of-function experiments provide evidence that
304 *MIRIAL* acts as a repressor of p53 signaling and interacts with p53. However, this pathway
305 does not contribute to the *MIRIAL*-mediated reduction of mitochondrial content.
306 Furthermore, the effects of *MIRIAL* silencing on endothelial quiescence, mitochondrial
307 activity and p53 signaling are independent of the co-expressed miR-23a, miR-27a and miR-
308 24-2.

309 **3.4. *MIRIAL* regulates endothelial quiescence through FOXO1 and MYC signaling**

310 To uncover the underlying mechanism by which *MIRIAL* regulates mitochondrial biogenesis,
311 we investigated the involvement of key transcription factors that govern endothelial
312 metabolism and quiescence, namely FOXO1 and MYC (also known as c-myc). FOXO1 and
313 MYC exhibit antagonistic roles in the endothelium. Under conditions lacking growth factor
314 stimulation, FOXO1 inhibits MYC signaling and promotes endothelial quiescence by
315 decreasing proliferation and metabolism[6]. However, upon stimulation with growth factors,
316 e.g. VEGF-A, this balance shifts towards enhanced MYC signaling. VEGF-A leads to an
317 increase of Akt kinase activity, resulting in phosphorylation of FOXO1, subsequent nuclear
318 export and proteasomal degradation[25].

319 By comparing gene sets of FOXO1 target genes (obtained from GSEA Molecular Signatures
320 Database C3 https://www.gsea-msigdb.org/gsea/msigdb/human/geneset/FOXO1_02.html)
321 and MYC mitochondrial target genes (obtained from[26]) to expression of all genes after
322 *MIRIAL* knockdown, we observed a robust downregulation (left-shift) of the FOXO1 target

323 genes, and an overall upregulation (right-shift) of mitochondrial target genes encoded in the
324 nucleus and controlled by MYC **(Fig. 4A)**.

325 After *MIRIAL* knockdown, we observed an increase in *MYC* expression in RNA-sequencing
326 **(Supp. Fig. 6A)**, qRT-PCR **(Fig. 4B)** and at protein level in Western blot **(Fig. 4C)**.
327 Simultaneously, *FOXO1* expression was decreased in RNA-sequencing **(Supp. Fig. 6B)**, qRT-
328 PCR **(Fig. 4D)** and at protein level **(Fig. 4E)**. Additionally, we found elevated levels of FOXO1
329 phosphorylation at Ser256 **(Fig. 4F)** and an increased ratio of phospho-FOXO1/total FOXO1
330 **(Fig. 4G)**. Both are indicative of inactivation, nuclear export, and subsequent degradation of
331 FOXO1. Activation of the anabolic transcription factor MYC leads to the exhaustion of
332 energy reserves, which in turn triggers the activation of AMP-activated kinase (AMPK), a key
333 sensor of cellular energy status[27]. Under conditions of a high AMP:ATP ratio, activated
334 AMPK can attenuate the cell cycle through p53 phosphorylation at Ser15 until energy stocks
335 are replenished[28, 29]. We assessed whether AMPK activation links MYC to the induction of
336 the p53 signaling pathway after *MIRIAL* knockdown using Western blot analysis. Protein
337 levels of AMPK **(Fig. 4H)** and its activated, phosphorylated (Thr172) form **(Fig. 4I)** were both
338 increased. MYC is a potent regulator of mitochondrial biogenesis and respiration[30, 31]. So, we
339 hypothesized that the upregulation of MYC after *MIRIAL* silencing is responsible for the
340 induction of mitochondrial function. To test this hypothesis, we performed siRNA-mediated
341 knockdown of MYC in conjunction with *MIRIAL* knockdown. The resulting abrogation of
342 *MIRIAL* depletion-mediated increase in mtDNA content demonstrated that MYC is indeed
343 essential for the regulation of mitochondrial biogenesis by *MIRIAL* **(Fig. 4J)**.

344 **3.5. *MIRIAL* forms *RNA*·DNA:DNA triplexes in the *FOXO1* promoter region**

345 Certain lncRNAs can act as epigenetic modifiers in a sequence-specific manner by forming
346 an *RNA*·DNA:DNA triplex with DNA. In this mechanism, a single-stranded lncRNA molecule
347 inserts into the major groove of the DNA double helix *via* Hoogsteen base pairing. This
348 structural arrangement enables the lncRNA to influence gene expression through chromatin
349 remodeling and recruitment of epigenetic modifiers[32, 33]. Examples include the lncRNAs
350 *Sarrah*[34] and *HIF1α-AS1*[35]. In our study, we observed that *MIRIAL* is primarily associated with
351 the chromatin in subcellular fractionation experiments **(Fig. 3A)**. Given its localization, we
352 investigated whether *MIRIAL* can form triplexes with double-stranded DNA. We analyzed
353 potential triplex-forming regions (TFRs) in *MIRIAL* using *TriplexAligner*[36] and found one
354 region within *MIRIAL* that has a high propensity for predicted triplex formation with double-
355 stranded DNA **(Fig. 5A)**. *MIRIAL* has previously been described as containing four
356 transposable elements that belong to the class of short, interspersed elements (SINEs),
357 more precisely, *Alu* elements[12]. The TFR we identified corresponds to the localization of the
358 first *Alu* element. Transposable elements, in particular *Alu* elements, have been proposed as
359 functional regions of lncRNAs before, e.g. for the lncRNAs S*MANTIS (*formerly known as
360 *MANTIS)*[37, 38] and *ANRIL*[39].

361 Further, we were interested to identify potential triplex target sites of *MIRIAL*. Employing
362 *TriplexAligner*[36], we predicted the triplex formation of *MIRIAL* with a selected list of
363 promoters of genes that were regulated following *MIRIAL* knockdown **(Fig. 5B)**. The *FOXO1*
364 promoter region emerged as the highest-scoring candidate in this preliminary, biased
365 analysis. In a more unbiased, genome-wide approach, we identified the top 50 enhancers
366 **(Fig. 5C)** (here denoted as regulatory elements (REMs) and annotated in EpiRegio
367 (https://epiregio.de/)[40, 41]) that are predicted to be target sites of *MIRIAL* triplex formation.
368 These regions were sorted based on their *TriplexAligner* scores (>50) and further stratified

369 based on coverage with active chromatin marks (H3K27ac) in endothelial cells obtained
370 from *ENCODE*[42]. This analysis provides a comprehensive view of the putative *MIRIAL* triplex
371 target-ome in human endothelial cells. Interestingly, the *MIRIAL-FOXO1* interaction is in the
372 top 0.15% of all predicted interactions with REMs and promoters combined and when
373 stratified by H3K27ac signal **(Supp. Fig. 6C)**. In addition, the putative *MIRIAL* triplex target
374 site in the *FOXO1* promoter region is not annotated as a transposable element **(Supp. Fig.**
375 **6D**, repeats track). However, it (a) is distinct from transcription factor binding sites at the
376 *FOXO1* promoter, (b) encompasses multiple REMs and (c) is an active regulatory region
377 highly enriched in H3K27ac and H3K4me3 histone marks, which are indicative of its likely
378 involvement in the control of *FOXO1* gene expression **(Supp. Fig. 6D)**.

379 To validate the functionality of *MIRIAL* as a triplex-forming RNA, we employed CRISPR/Cas9
380 to delete the *MIRIAL* TFR from its genomic locus. As the predicted TFR is located within a
381 stretch of repetitive elements, guide RNAs (gRNAs) were strategically designed for the
382 regions both upstream and downstream of the *Alu* sequence. This targeted knockout
383 strategy resulted in the deletion of 1016 bp **(Fig. 5D)**. We confirmed the knockout in HUVECs
384 by genomic DNA PCR **(Fig. 5E)** and qRT-PCR **(Fig. 5F)**. Our findings indicate that the excision
385 of the transposable elements - including the predicted TFR - from the *MIRIAL* locus results in
386 a downregulation of *FOXO1* **(Fig. 5G)** and an upregulation of *MYC* expression **(Fig. 5H)**, a
387 change comparable to the effects observed following depletion of the full-length *MIRIAL*
388 transcript **(Fig. 2G)**. Furthermore, removal of the TFR triggered an increase of mtDNA
389 content in the cells **(Fig. 5I)**. Our results provide evidence that the four transposable
390 elements within *MIRIAL* harbor a functional region, that appears to influence gene
391 expression and mitochondrial biogenesis, potentially through a direct interaction with
392 chromatin.

393 **3.6. *MIRIAL* recruits Mortality Factor 4 Like 2 (MORF4L2) and TATA-binding Protein-**
394 **associated Factor 2N (TAF15) to the *FOXO1* transcriptional start site**

395 To assess the mechanism underlying the transcriptional activation of *FOXO1* by *MIRIAL*, we
396 used RNA pulldown followed by mass spectrometry to identify protein interaction partners
397 of *MIRIAL*. Our findings validated the interaction of the RNA helicase DDX5/p68 and *MIRIAL*
398 in endothelial cells, which had previously been described in HEK293T cells[12]. Among the
399 enriched proteins, we identified MORF4L2 as a potential interactor of *MIRIAL* **(Fig. 6A)**.
400 MORF4L2 (also known as MRGX) is a component of the NuA4 histone acetyltransferase
401 (HAT) complex[43]. This highly conserved complex is a recognized transcriptional regulator of
402 *FOXO1* in HeLa cells and of the FOXO transcription factor *daf-16* in *C. elegans*. In both
403 species, it has been linked to oxidative stress resistance and contributes to longevity in *C.*
404 *elegans*[44]. Interestingly, other proteins from this HAT complex (the helicases RUVBL1 and 2,
405 ACTB and ACTL6A/BAF53) were found in the RNA pulldown, although they were not
406 enriched to the same level as MORF4L2.

407 We confirmed the interaction between MORF4L2 and *MIRIAL* by CLIP **(Fig. 6B)**. siRNA-
408 mediated knockdown of *MORF4L2* **(Fig. 6C and Supp. Fig. 7A)** resulted in a significant
409 upregulation of mtDNA content **(Fig. 6D)**, comparable to the previously observed effect of
410 *MIRIAL* silencing **(Fig. 2G)**. Additionally, an upregulation of *MYC* could be observed following
411 MORF4L2 depletion **(Fig. 6E)**, but there was no discernable downregulation of *FOXO1*
412 expression **(Fig. 6F)**. Knockdown of *MORF4L2* was sufficient to upregulate the expression of
413 another potential protein interactor of *MIRIAL*, TAF15 **(Fig. 6A and 6G)**. This protein is a
414 component of the transcription initiation factor $TF_{II}D$ complex which makes up part of the
415 RNA polymerase II pre-initiation complex[45]. The upregulation of *TAF15* could potentially

416 compensate for the loss of *MORF4L2*. Of note, neither *TAF15* nor *MORF4L2* expression were
417 changed following *MIRIAL* knockdown **(Supp. Fig. 7B and 7C)**. However, a knockdown of
418 *TAF15* using siRNA **(Supp. Fig. 7D and 7E)** alongside *MORF4L2* knockdown was sufficient to
419 significantly reduce *FOXO1* expression **(Fig. 6H)** to similar levels as *MIRIAL* knockdown.
420 Moreover, mtDNA content **(Fig. 6I)** and *MYC* expression **(Fig. 6J)** were increased after the
421 double knockdown of *TAF15* and *MORF4L2*, confirming that both proteins are essential for
422 the effects of *MIRIAL* on mitochondria.

423 To verify that *MIRIAL* recruits MORF4L2 and the NuA4 complex to the *FOXO1* transcriptional
424 start site we performed chromatin immunoprecipitation (ChIP) using a MORF4L1/2 antibody
425 and measured the *FOXO1* promoter sequence in the precipitate by qPCR. We found that
426 MORF4L1/2 interact with the *FOXO1* promoter region **(Fig. 6K)**, and that this interaction was
427 reduced after silencing of *MIRIAL* **(Fig. 6K)** showing that *MIRIAL* helps guiding the NuA4
428 complex to its genomic target site.

429 In conclusion, *MIRIAL* interacts with MORF4L2, a component of the NuA4 histone
430 acetyltransferase complex. Through this interaction *MIRIAL* guides this HAT complex to the
431 *FOXO1* promoter region to facilitate *FOXO1* transcription.

432 *3.7. Mirial* KO in mice decreases EF after acute myocardial infarction and regulates 433 angiogenic sprouting *ex vivo*

434 Having elucidated the molecular mechanism of *MIRIAL* in HUVECs, we questioned whether
435 *Mirial* depletion would have any *in vivo* consequences in a mouse model. To determine its
436 involvement in angiogenesis *in vivo*, we created a *Mirial* knockout (KO) mouse line utilizing
437 CRISPR/Cas9 **(Supp. Fig. 8A)**. We confirmed the successful deletion of *Mirial* in these mice
438 **(Supp. Fig. 8B)**, while the expression of the adjacent miRNA cluster remained unaffected

439 **(Supp. Fig. 8C)**. *Mirial* KO mice exhibited normal viability, fertility and showed no apparent
440 basal defects. Interestingly, in contrast to the *in vitro* findings in HUVECs, we observed that
441 the deletion of *Mirial* did not result in an elevation of mitochondrial content in the hearts of
442 young or aged *Mirial* KO mice compared to their wild-type littermates **(Fig. 7A)**.

443 To evaluate the impact of *Mirial* KO on the restoration of myocardial capillarization and
444 perfusion post-injury, we conducted acute myocardial infarction (AMI) surgery, followed by
445 echocardiographic assessment of cardiac function and histological examination of the heart.
446 Echocardiography was performed on the first day post-surgery, as well as at two- and four-
447 weeks post-surgery **(Supp. Fig. 8D)**. Comparing the change of contractile function (ΔEF) from
448 the first day post-surgery to the four-week endpoint revealed a significantly reduced
449 ejection fraction in *Mirial* knockout animals **(Fig. 7B)**.

450 To assess the effects of *Mirial* loss on the cardiac phenotype following AMI at the cellular
451 level, we performed immunohistochemical staining of serial sections of the heart **(Supp. Fig.
452 8E)**. Capillary density analysis revealed no change in number, size, or perimeter **(Fig. 7C-7E)**
453 of capillaries in the border zone of AMI heart sections. Moreover, histological examination
454 following Sirius Red staining of collagen showed no significant alterations in infarct size or
455 fibrosis after *Mirial* knockout **(Supp. Fig. 8F-8H)**.

456 Next, *ex vivo* angiogenic capacity was tested using the aortic ring assay with aortic samples
457 from both young (3 months) and aged (18 months) **(Fig. 7F and 7G)** mice. In old animals
458 basal sprouting was drastically reduced after *Mirial* KO. Additionally, confirming our
459 previous observations of the *in vitro* sprouting assay, these *ex vivo* experiments show that
460 endothelial cells from *Mirial* KO animals exhibit increased responsiveness to VEGF-A in in
461 both age brackets.

462 Together, these experiments show that loss of *Mirial in vivo* has an adverse effect on cardiac
463 outcome after AMI. Moreover, *Mirial* is an important regulator of VEGF-A-response and
464 angiogenic sprouting *in vitro* and *ex vivo*.

465

466 **4. Discussion**

467 The present study reveals that the aging-induced lncRNA *MIRIAL* promotes endothelial cell
468 proliferation and migration, while reducing mitochondrial mass, spare respiratory capacity
469 and p53 signaling through modulation of the FOXO1-MYC antagonism, desensitizing
470 endothelial cells against VEGF-A signaling.

471 In the present study, *MIRIAL* knockdown in HUVECs and *Mirial* knockout in mice had
472 divergent effects on angiogenic sprouting if VEGF-A was administered compared to basal
473 conditions. Under unstimulated conditions loss of *MIRIAL* decreases sprouting. This
474 phenotype can be attributed to the accompanying induction of the p53 pathway and
475 reduction in migration and proliferation. However, we show that VEGF-A administration not
476 only rescues the effect of *MIRIAL* knockdown on proliferation, but also leads to
477 overshooting angiogenic sprouting, both *in vitro* and *ex vivo*. We hypothesize that this is due
478 to a strong induction of MYC through VEGFR2 signaling[46], which overrules the effects of p53
479 signaling.

480 While there was no change in capillarization, infarct size or fibrosis after AMI, a noticeable
481 reduction in the change of ejection fraction was observed. This may be due to an as-yet-
482 undefined function of *Mirial* in cardiomyocytes, which could potentially enhance or protect
483 contractile function after AMI.

484 In mice, decreased expression of *Mirial* has been linked to reduced FoxO signaling[8]. In our
485 *Mirial* KO mouse model, the regulation of FoxO signaling could not be confirmed. Comparing
486 the human and mouse orthologues of *MIRIAL* shows that the mouse transcript is
487 significantly shorter than the human orthologue (690 bp versus 1774 bp) and lacks the *Alu*
488 element-containing region, as *Alu* elements are only conserved in primates[47]. We conclude

489 that human *MIRIAL* and mouse *Mirial* are only partially functionally conserved, and that
490 human *MIRIAL* alters gene expression *via* a triplex-dependent mechanism that is not evident
491 in mice.

492 The putative TFR of *MIRIAL*, that is predicted to interact with the *FOXO1* promoter region,
493 contains an *Alu* element. Interestingly, lncRNAs, like S*MANTIS*[37, 38] and *ANRIL*[39], were
494 described to contain *Alu* elements as functional regions and were shown to regulate
495 endothelial cell function and atherogenesis. The lncRNA *KCNQ1OT1* contains a transposable
496 element of the L1 class capable of forming a triplex with L1 and *Alu* elements on genomic
497 DNA[48]. However, unlike the aforementioned examples, our study is the first to describe a
498 triplex-forming *Alu* element within a lncRNA. This unique feature sets *MIRIAL* apart from
499 other lncRNAs that have been studied until now.

500 **Conclusion**

501 Taken together, *MIRIAL* is an aging-induced lncRNA which acts as a key regulator of
502 endothelial metabolic and cellular function. *MIRIAL* promotes cell proliferation, migration
503 and basal angiogenic sprouting while decreasing mitochondrial function. However, silencing
504 *MIRIAL* in pro-angiogenic conditions improves angiogenesis. We hypothesize that *MIRIAL*
505 influences these cellular functions by affecting the p53 pathway and mitochondrial
506 respiration through FOXO1 signaling. These results suggest that transcriptional modulation
507 of *MIRIAL*, particularly in the elderly, might be a promising strategy to improve therapeutic
508 angiogenesis.

509 **Acknowledgments and sources of funding**

510 This work was supported by the Goethe University Frankfurt/Main, Germany; the Deutsche
511 Forschungsgemeinschaft (DFG) excellence cluster EXS2026 (Cardio-Pulmonary Institute)
512 [project number 390649896]; the Deutsche Forschungsgemeinschaft (DFG) Transregio
513 project TRR267 [project number 403584255, project B04 to RAB and LM, project B03 and
514 A01 to SD, project A04 to MSL, project A06 to RPB, and project Z02 to IW]; the Deutsche
515 Forschungsgemeinschaft (DFG) collaborative research centre SFB 834 [project number
516 75732319, project B09 to RAB); the German Centre for Cardiovascular Research (DZHK); an
517 European Research Council (ERC) starting grant (NOVA) [project number 638178]; and an
518 European Research Council (ERC) consolidator grant (NICCA) [project number 101002599].
519 The graphical abstract was created with BioRender.com.

520 **Author contributions**

521 CK, KT, and RAB conceptualized and designed the study. CK, SK, TW, KT, AF, RPJ, MMR, DB,
522 FL, FV, JUGW, JS, ATG, LS, SG, IW, LM and MSL acquired, analyzed, and interpreted data. CK
523 drafted the manuscript. All authors critically revised the manuscript and approved the final
524 version to be published.

525 **Conflict of Interest:** non declared.

526 **List of Supplementary Data:**

527 1. Supplementary Figures and Legends 1-8
528 2. Supplementary Methods
529 3. Supplementary Tables 1-5
530 4. Supplementary References

531 **References**

532 1. Boon RA, Jaé N, Holdt L, Dimmeler S. Long noncoding rnas: From clinical genetics to
533 therapeutic targets? *J Am Coll Cardiol*. 2016;**67**:1214-1226
534 2. Quinn JJ, Chang HY. Unique features of long non-coding rna biogenesis and function. *Nat Rev*
535 *Genet*. 2016;**17**:47-62
536 3. Mc Namara K, Alzubaidi H, Jackson JK. Cardiovascular disease as a leading cause of death:
537 How are pharmacists getting involved? *Integr Pharm Res Pract*. 2019;**8**:1-11
538 4. Niccoli T, Partridge L. Ageing as a risk factor for disease. *Current Biology*. 2012;**22**:R741-R752
539 5. Abdellatif M, Rainer PP, Sedej S, Kroemer G. Hallmarks of cardiovascular ageing. *Nat Rev*
540 *Cardiol*. 2023;**20**:754-777
541 6. Wilhelm K, Happel K, Eelen G, Schoors S, Oellerich MF, Lim R, Zimmermann B, Aspalter IM,
542 Franco CA, Boettger T, Braun T, Fruttiger M, Rajewsky K, Keller C, Brüning JC, Gerhardt H,
543 Carmeliet P, Potente M. Foxo1 couples metabolic activity and growth state in the vascular
544 endothelium. *Nature*. 2016;**529**:216-220
545 7. Paik J-H, Kollipara R, Chu G, Ji H, Xiao Y, Ding Z, Miao L, Tothova Z, Horner JW, Carrasco DRJC.
546 Foxos are lineage-restricted redundant tumor suppressors and regulate endothelial cell
547 homeostasis. *Cell*. 2007;**128**:309-323
548 8. Fan J, Zhou Q, Li Y, Song X, Hu J, Qin Z, Tang J, Tao T. Profiling of long non-coding rnas and
549 mrnas by rna-sequencing in the hippocampi of adult mice following propofol sedation. *Front*
550 *Mol Neurosci*. 2018;**11**:91
551 9. Fan C, Tang Y, Wang J, Wang Y, Xiong F, Zhang S, Li X, Xiang B, Wu X, Guo C, Ma J, Zhou M, Li
552 X, Xiong W, Li Y, Li G, Zeng Z. Long non-coding rna loc284454 promotes migration and
553 invasion of nasopharyngeal carcinoma via modulating the rho/rac signaling pathway.
554 *Carcinogenesis*. 2019;**40**:380-391
555 10. Han L, Zhou W, Wu F. Long non□coding rna loc284454 promotes hepatocellular carcinoma
556 cell invasion and migration by inhibiting e□cadherin expression. *Oncol Rep*. 2021;**45**
557 11. Liu H, Gu X, Wang G, Huang Y, Ju S, Huang J, Wang X. Copy number variations primed lncrnas
558 deregulation contribute to poor prognosis in colorectal cancer. *Aging (Albany NY)*.
559 2019;**11**:6089-6108
560 12. Das M, Renganathan A, Dighe SN, Bhaduri U, Shettar A, Mukherjee G, Kondaiah P,
561 Satyanarayana Rao MR. Ddx5/p68 associated lncrna loc284454 is differentially expressed in
562 human cancers and modulates gene expression. *RNA Biol*. 2018;**15**:214-230
563 13. Fan C, Wang J, Tang Y, Zhang S, Xiong F, Guo C, Zhou Y, Li Z, Li X, Li Y, Li G, Zeng Z, Xiong W.
564 Upregulation of long non-coding rna loc284454 may serve as a new serum diagnostic
565 biomarker for head and neck cancers. *BMC Cancer*. 2020;**20**:917
566 14. Bonauer A, Carmona G, Iwasaki M, Mione M, Koyanagi M, Fischer A, Burchfield J, Fox H,
567 Doebele C, Ohtani K, Chavakis E, Potente M, Tjwa M, Urbich C, Zeiher AM, Dimmeler S.
568 Microrna-92a controls angiogenesis and functional recovery of ischemic tissues in mice.
569 *Science*. 2009;**324**:1710-1713
570 15. Gimbel AT, Koziarek S, Theodorou K, Schulz JF, Stanicek L, Ali T, Günther S, Kumar S, Jo H,
571 Hübner N, Maegdefessel L, Dimmeler S, van Heesch S, Boon RA. Aging-regulated tug1 is
572 dispensable for endothelial cell function. *PLoS One*. 2022:2022.2002.2027.482212
573 16. [dataset], Fasolo F, Winski G, Li Z, Wu Z, Winter H, Ritzer J, Glukha N, Roy J, Hultgren R, Pauli
574 J, Busch A, Sachs N, Knappich C, Eckstein HH, Boon RA, Paloschi V, Maegdefessel L. The
575 circular rna ataxia telangiectasia mutated regulates oxidative stress in smooth muscle cells in
576 expanding abdominal aortic aneurysms. *Mol Ther Nucleic Acids*. 2023;**33**:848-865; Gene
577 Expression Omnibus accession number GSE237230
578 17. [dataset], Wagner JUG, Tombor LS, Malacarne PF, Kettenhausen L-M, Panthel J, Kujundzic H,
579 Manickam N, Schmitz K, Cipca M, Stilz KA, Fischer A, Muhly-Reinholz M, Abplanalp WT, John
580 D, Mohanta SK, Weber C, Habenicht AJR, Buchmann GK, Angendohr S, Amin E, Scherschel K,

581 Klöcker N, Kelm M, Schüttler D, Clauss S, Günther S, Boettger T, Braun T, Bär C, Pham M-D,
582 Krishnan J, Hille S, Müller OJ, Bozoglu T, Kupatt C, Nardini E, Osmanagic-Myers S, Meyer C,
583 Zeiher AM, Brandes RP, Luxán G, Dimmeler S. Aging impairs the neurovascular interface in
584 the heart. *Science*. 2023;**381**:897-906; doi:810.1126/science.ade4961
585 18. [dataset], Drekolia MK, Talyan S, Cordellini Emídio R, Boon RA, Guenther S, Looso M,
586 Dumbović G, Bibli SI. Unravelling the impact of aging on the human endothelial lncrna
587 transcriptome. *Front Genet*. 2022;**13**:1035380;
588 doi:1035310.1033389/fgene.1032022.1035380
589 19. Huang X, Miller W. A time-efficient, linear-space local similarity algorithm. *Adv Appl Math*.
590 1991;**12**:337-357
591 20. Wang L, Park HJ, Dasari S, Wang S, Kocher JP, Li W. Cpat: Coding-potential assessment tool
592 using an alignment-free logistic regression model. *Nucleic Acids Res*. 2013;**41**:e74
593 21. De Bock K, Georgiadou M, Schoors S, Kuchnio A, Wong Brian W, Cantelmo Anna R,
594 Quaegebeur A, Ghesquière B, Cauwenberghs S, Eelen G, Phng L-K, Betz I, Tembuyser B,
595 Brepoels K, Welti J, Geudens I, Segura I, Cruys B, Bifari F, Decimo I, Blanco R, Wyns S,
596 Vangindertael J, Rocha S, Collins Russel T, Munck S, Daelemans D, Imamura H, Devlieger R,
597 Rider M, Van Veldhoven Paul P, Schuit F, Bartrons R, Hofkens J, Fraisl P, Telang S,
598 DeBerardinis Ralph J, Schoonjans L, Vinckier S, Chesney J, Gerhardt H, Dewerchin M,
599 Carmeliet P. Role of pfkfb3-driven glycolysis in vessel sprouting. *Cell*. 2013;**154**:651-663
600 22. Youle RJ, van der Bliek AM. Mitochondrial fission, fusion, and stress. *Science*. 2012;**337**:1062-
601 1065
602 23. Colman MS, Afshari CA, Barrett JC. Regulation of p53 stability and activity in response to
603 genotoxic stress. *Mutation Research/Reviews in Mutation Research*. 2000;**462**:179-188
604 24. Fiedler J, Jazbutyte V, Kirchmaier BC, Gupta SK, Lorenzen J, Hartmann D, Galuppo P, Kneitz S,
605 Pena JTG, Sohn-Lee C, Loyer X, Soutschek J, Brand T, Tuschl T, Heineke J, Martin U, Schulte-
606 Merker S, Ertl G, Engelhardt S, Bauersachs J, Thum T. Microrna-24 regulates vascularity after
607 myocardial infarction. *Circulation*. 2011;**124**:720-730
608 25. Greer EL, Brunet A. Foxo transcription factors at the interface between longevity and tumor
609 suppression. *Oncogene*. 2005;**24**:7410-7425
610 26. Morrish F, Hockenbery D. Myc and mitochondrial biogenesis. *Cold Spring Harb Perspect*
611 *Med*. 2014;**4**
612 27. Liu L, Ulbrich J, Müller J, Wüstefeld T, Aeberhard L, Kress TR, Muthalagu N, Rycak L, Rudalska
613 R, Moll R, Kempa S, Zender L, Eilers M, Murphy DJ. Deregulated myc expression induces
614 dependence upon ampk-related kinase 5. *Nature*. 2012;**483**:608-612
615 28. Jones RG, Plas DR, Kubek S, Buzzai M, Mu J, Xu Y, Birnbaum MJ, Thompson CB. Amp-
616 activated protein kinase induces a p53-dependent metabolic checkpoint. *Mol Cell*.
617 2005;**18**:283-293
618 29. Kruse JP, Gu W. Snapshot: P53 posttranslational modifications. *Cell*. 2008;**133**:930-930.e931
619 30. Li F, Wang Y, Zeller KI, Potter JJ, Wonsey DR, O'Donnell KA, Kim JW, Yustein JT, Lee LA, Dang
620 CV. Myc stimulates nuclearly encoded mitochondrial genes and mitochondrial biogenesis.
621 *Mol Cell Biol*. 2005;**25**:6225-6234
622 31. Goetzman ES, Prochownik EV. The role for myc in coordinating glycolysis, oxidative
623 phosphorylation, glutaminolysis, and fatty acid metabolism in normal and neoplastic tissues.
624 *Front Endocrinol (Lausanne).* 2018;**9**
625 32. Hoogsteen K. The structure of crystals containing a hydrogen-bonded complex of 1-
626 methylthymine and 9-methyladenine. *Acta crystallographica*. 1959;**12**:822-823
627 33. Rajagopal P, Feigon J. Triple-strand formation in the homopurine:Homopyrimidine DNA
628 oligonucleotides d(g-a)4 and d(t-c)4. *Nature*. 1989;**339**:637-640
629 34. Trembinski DJ, Bink DI, Theodorou K, Sommer J, Fischer A, van Bergen A, Kuo CC, Costa IG,
630 Schürmann C, Leisegang MS, Brandes RP, Alekseeva T, Brill B, Wietelmann A, Johnson CN,
631 Spring-Connell A, Kaulich M, Werfel S, Engelhardt S, Hirt MN, Yorgan K, Eschenhagen T,

632 Kirchhof L, Hofmann P, Jaé N, Wittig I, Hamdani N, Bischof C, Krishnan J, Houtkooper RH,
633 Dimmeler S, Boon RA. Aging-regulated anti-apoptotic long non-coding rna sarrah augments
634 recovery from acute myocardial infarction. *Nat Comm*. 2020;**11**:2039
635 35. Leisegang MS, Bains JK, Seredinski S, Oo JA, Krause NM, Kuo CC, Günther S, Sentürk Cetin N,
636 Warwick T, Cao C, Boos F, Izquierdo Ponce J, Haydar S, Bednarz R, Valasarajan C, Fuhrmann
637 DC, Preussner J, Looso M, Pullamsetti SS, Schulz MH, Jonker HRA, Richter C, Rezende F,
638 Gilsbach R, Pflüger-Müller B, Wittig I, Grummt I, Ribarska T, Costa IG, Schwalbe H, Brandes
639 RP. Hif1α-as1 is a DNA:DNA:Rna triplex-forming lncrna interacting with the hush complex.
640 *Nat Comm*. 2022;**13**:6563
641 36. Warwick T, Seredinski S, Krause NM, Bains JK, Althaus L, Oo JA, Bonetti A, Dueck A,
642 Engelhardt S, Schwalbe H, Leisegang MS, Schulz MH, Brandes RP. A universal model of
643 rna.DNA:DNA triplex formation accurately predicts genome-wide rna-DNA interactions. *Brief*
644 *Bioinform*. 2022;**23**
645 37. Leisegang MS, Fork C, Josipovic I, Richter FM, Preussner J, Hu J, Miller MJ, Epah J, Hofmann
646 P, Günther S, Moll F, Valasarajan C, Heidler J, Ponomareva Y, Freiman TM, Maegdefessel L,
647 Plate KH, Mittelbronn M, Uchida S, Künne C, Stellos K, Schermuly RT, Weissmann N, Devraj
648 K, Wittig I, Boon RA, Dimmeler S, Pullamsetti SS, Looso M, Miller FJ, Jr., Brandes RP. Long
649 noncoding rna mantis facilitates endothelial angiogenic function. *Circulation*. 2017;**136**:65-
650 79
651 38. Leisegang MS, Bibli S-I, Günther S, Pflüger-Müller B, Oo JA, Höper C, Seredinski S, Yekelchyk
652 M, Schmitz-Rixen T, Schürmann C, Hu J, Looso M, Sigala F, Boon RA, Fleming I, Brandes RP.
653 Pleiotropic effects of laminar flow and statins depend on the krüppel-like factor-induced
654 lncrna mantis. *Eur Heart J*. 2019;**40**:2523-2533
655 39. Holdt LM, Hoffmann S, Sass K, Langenberger D, Scholz M, Krohn K, Finstermeier K, Stahringer
656 A, Wilfert W, Beutner F, Gielen S, Schuler G, Gäbel G, Bergert H, Bechmann I, Stadler PF,
657 Thiery J, Teupser D. Alu elements in anril non-coding rna at chromosome 9p21 modulate
658 atherogenic cell functions through trans-regulation of gene networks. *PLoS Genet*.
659 2013;**9**:e1003588
660 40. Baumgarten N, Hecker D, Karunanithi S, Schmidt F, List M, Schulz MH. Epiregio: Analysis and
661 retrieval of regulatory elements linked to genes. *Nucleic Acids Research*. 2020;**48**:W193-
662 W199
663 41. Schmidt F, Marx A, Baumgarten N, Hebel M, Wegner M, Kaulich M, Leisegang Matthias S,
664 Brandes Ralf P, Göke J, Vreeken J, Schulz Marcel H. Integrative analysis of epigenetics data
665 identifies gene-specific regulatory elements. *Nucleic Acids Research*. 2021;**49**:10397-10418
666 42. Davis CA, Hitz BC, Sloan CA, Chan ET, Davidson JM, Gabdank I, Hilton JA, Jain K, Baymuradov
667 UK, Narayanan AK, Onate KC, Graham K, Miyasato SR, Dreszer TR, Strattan J S, Jolanki O,
668 Tanaka FY, Cherry J M. The encyclopedia of DNA elements (encode): Data portal update.
669 *Nucleic Acids Research*. 2017;**46**:D794-D801
670 43. Devoucoux M, Roques C, Lachance C, Lashgari A, Joly-Beauparlant C, Jacquet K, Alerasool N,
671 Prudente A, Taipale M, Droit A, Lambert J-P, Hussein SMI, Côté J. Mrg proteins are shared by
672 multiple protein complexes with distinct functions. *Mol Cell Proteomics*. 2022;**21**:100253
673 44. Ikeda T, Uno M, Honjoh S, Nishida E. The myst family histone acetyltransferase complex
674 regulates stress resistance and longevity through transcriptional control of daf-16/foxo
675 transcription factors. *EMBO Rep*. 2017;**18**:1716-1726
676 45. Bertolotti A, Lutz Y, Heard DJ, Chambon P, Tora L. Htaf(ii)68, a novel rna/ssdna-binding
677 protein with homology to the pro-oncoproteins tls/fus and ews is associated with both tfiid
678 and rna polymerase ii. *EMBO J*. 1996;**15**:5022-5031
679 46. Dang Chi V. Myc on the path to cancer. *Cell*. 2012;**149**:22-35
680 47. Deininger P. Alu elements: Know the sines. *Genome Biology*. 2011;**12**:236

681 48. Zhang X, Jiang Q, Li J, Zhang S, Cao Y, Xia X, Cai D, Tan J, Chen J, Han J-DJ. Kcnq1ot1 promotes
682 genome-wide transposon repression by guiding rna–DNA triplexes and hp1 binding. *Nat Cell*
683 *Biol*. 2022;**24**:1617-1629

684

685

686 **Figures**

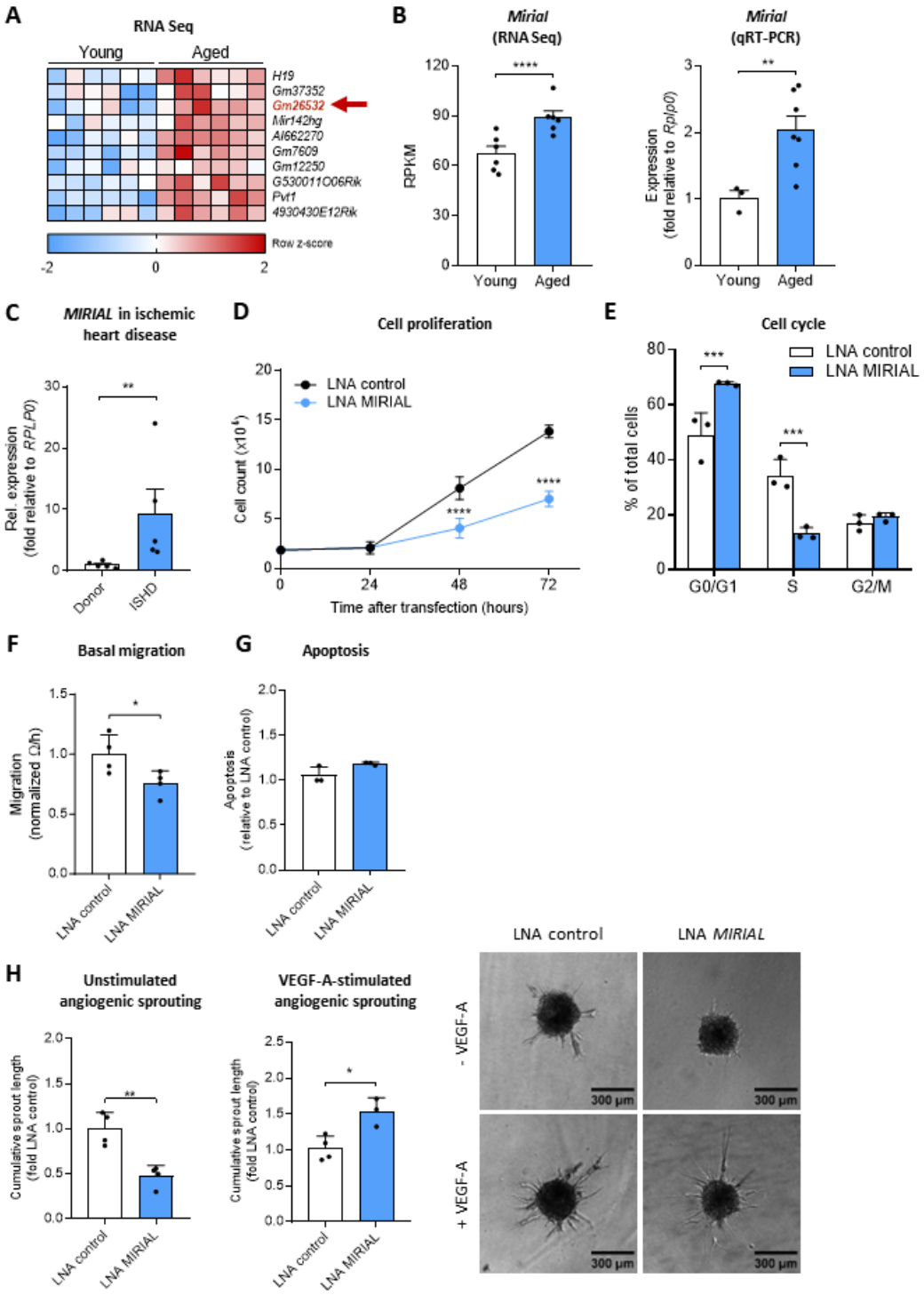

687

688 **Fig. 1: *MIRIAL* is an aging-induced long non-coding RNA that regulates endothelial cell**

689 **quiescence**

690 **A** Heatmap representing the most significant differentially regulated lncRNAs from RNA-
691 sequencing data of cardiac ECs isolated from young (12 weeks) and aged (20 months) mice
692 (*n*=6). **B** *Mirial* expression from RNA seq data (*n*=6; Mann-Whitney test with FDR correction)
693 quantified from fig. 1 A and *Mirial* expression from aortic intima of young (12 weeks) and
694 aged mice (20 months) measured by qRT-PCR (n=3 and 7; Welch's *t* test). Results are
695 expressed as mean ± s.e.m. **C** *MIRIAL* expression in ischemic heart disease cardiac biopsies
696 compared to healthy controls measured by qRT-PCR (*n*=5; Mann-Whitney test). Results are
697 expressed as mean ± s.e.m. **D** Growth curve depicting the cell number of HUVECs after the
698 indicated hours (0-72h) of gapmeR-mediated *MIRIAL* knockdown (20 nM) compared to
699 control-transfected HUVECs (representative graph of *n*=3; ANOVA). **E** EdU combined with
700 FxCycle flow cytometry-based cell cycle analysis of HUVECs 48h after gapmeR-mediated
701 *MIRIAL* knockdown (20 nM) compared to control-transfected HUVECs (*n*=3; ANOVA). **F**
702 Electric cell-substrate impedance sensing (ECIS)-based migration assay of HUVECs 48h after
703 gapmeR-mediated *MIRIAL* knockdown (20 nM) compared to control-transfected HUVECs
704 (*n*=4; unpaired *t* test). **G** Caspase 3/7 activity-based apoptosis assay of HUVECs 48h after
705 gapmeR-mediated *MIRIAL* knockdown (20 nM) compared to control-transfected HUVECs
706 (*n*=3; unpaired *t* test). **H** Cumulative sprout length in an angiogenic spheroid sprouting assay
707 under basal and VEGF-stimulated (50 ng/mL) conditions using HUVECs 72h after gapmeR-
708 mediated *MIRIAL* knockdown (20 nM) compared to control-transfected HUVECs (*n*=4;
709 unpaired *t* test). 8-15 spheroids per condition were analyzed. Results are expressed as mean
710 ± s.d. unless otherwise stated; *$p<0.05$, **$p<0.01$, ***$p<0.001$, **** $p<0.0001$

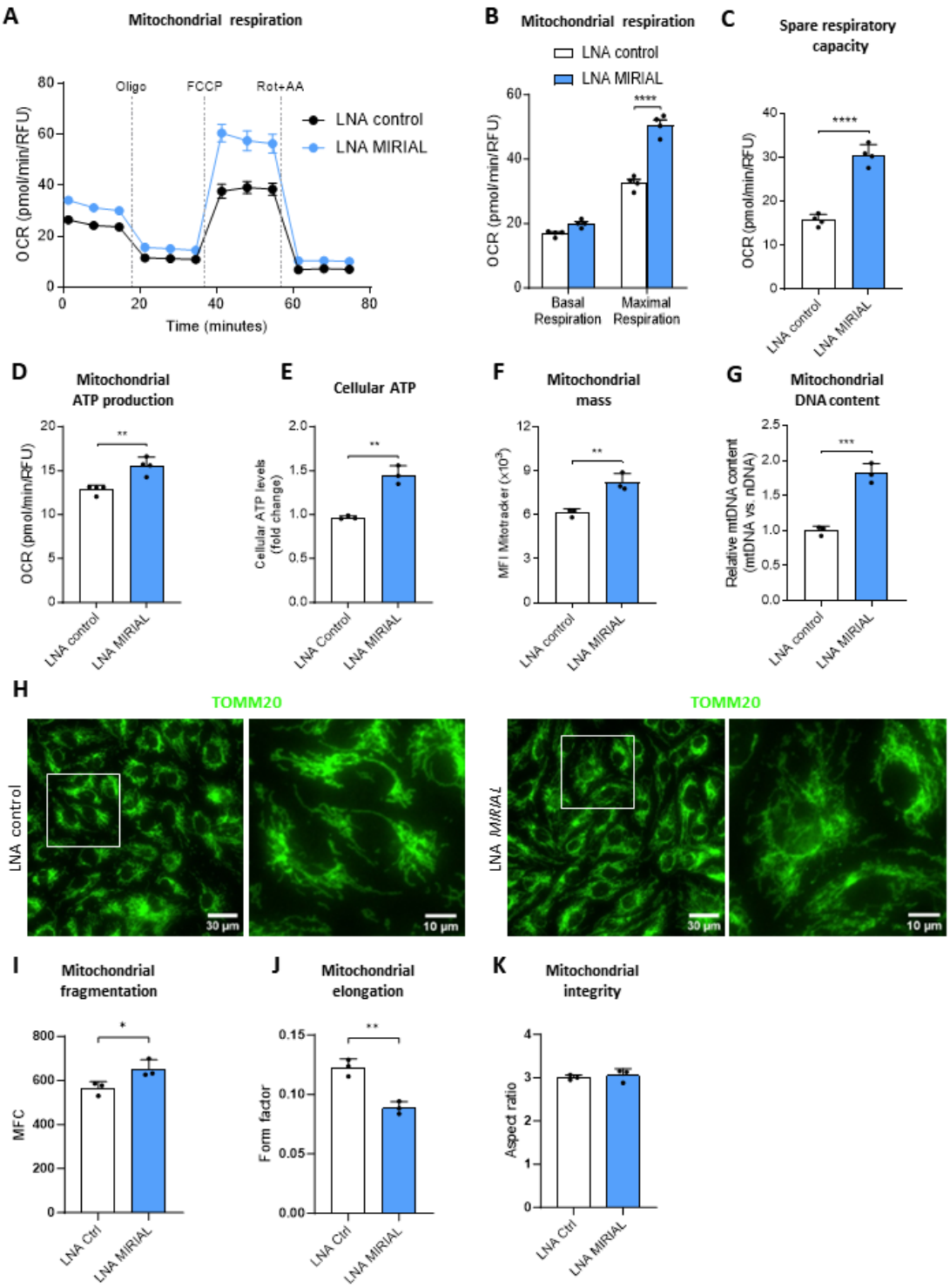

Fig. 2: *MIRIAL* regulates endothelial mitochondrial metabolism

A Oxygen consumption rate (OCR) as a measure of mitochondrial respiration in HUVECs 48h after gapmeR-mediated *MIRIAL* knockdown (20 nM) compared to control-transfected

715 HUVECs using Seahorse mitochondrial stress test (representative graph of *n*=4). **B** Oxygen
716 consumption rate (OCR) as a measure of mitochondrial basal and maximal respiration in
717 HUVECs 48h after gapmeR-mediated *MIRIAL* knockdown (20 nM) compared to control-
718 transfected HUVECs, quantified from fig. 2 A using Seahorse mitochondrial stress test (*n*=4;
719 ANOVA). **C** Spare respiratory capacity (SRC) of HUVECs 48h after gapmeR-mediated *MIRIAL*
720 knockdown (20 nM) compared to control-transfected HUVECs, quantification from fig. 4A
721 (*n*=4; unpaired *t* test). **D** Mitochondrial ATP production of HUVECs 48h after gapmeR-
722 mediated *MIRIAL* knockdown (20 nM) compared to control-transfected HUVECs using
723 Seahorse mitochondrial stress test (*n*=4; unpaired *t* test). **E** Cellular ATP levels of HUVECs 48h
724 after gapmeR-mediated *MIRIAL* knockdown (20 nM) compared to control-transfected
725 HUVECs using bioluminescence-based assay (*n*=3). **F** Mitochondrial mass of HUVECs 48h
726 after gapmeR-mediated *MIRIAL* knockdown (20 nM) compared to control-transfected
727 HUVECs measured by Mitotracker flow cytometry (*n*=3; unpaired *t* test). **G** Mitochondrial
728 DNA (mtDNA) content relative to nuclear DNA (nDNA) content of HUVECs 48h after gapmeR-
729 mediated *MIRIAL* knockdown (20 nM) compared to control-transfected HUVECs using qPCR
730 (*n*=3; unpaired *t* test). **H** Representative images of HUVECs 48h after gapmeR-mediated
731 *MIRIAL* knockdown (20 nM) compared to control-transfected HUVECs stained with an
732 TOMM20 antibody and analyzed by immunofluorescence microscopy. **I** Mitochondrial
733 fragmentation count (MFC) in HUVECs 48h after gapmeR-mediated *MIRIAL* knockdown (20
734 nM) compared to control-transfected HUVECs stained with an TOMM20 antibody and
735 analyzed by immunofluorescence microscopy (*n*=3; unpaired *t* test). **J** Mitochondrial
736 elongation measured as mitochondrial form factor in HUVECs 48h after gapmeR-mediated
737 *MIRIAL* knockdown (20 nM) compared to control-transfected HUVECs stained with an
738 TOMM20 antibody and analyzed by immunofluorescence microscopy (*n*=3; unpaired *t* test).

739 **K** Mitochondrial integrity in HUVECs 48h after gapmeR-mediated *MIRIAL* knockdown (20
740 nM) compared to control-transfected HUVECs stained with an TOMM20 antibody and
741 analyzed by immunofluorescence microscopy (n=3; unpaired t test). Results are expressed as
742 mean ± s.d.; *p<0.05, **p<0.01, ***p<0.001, **** p<0.0001

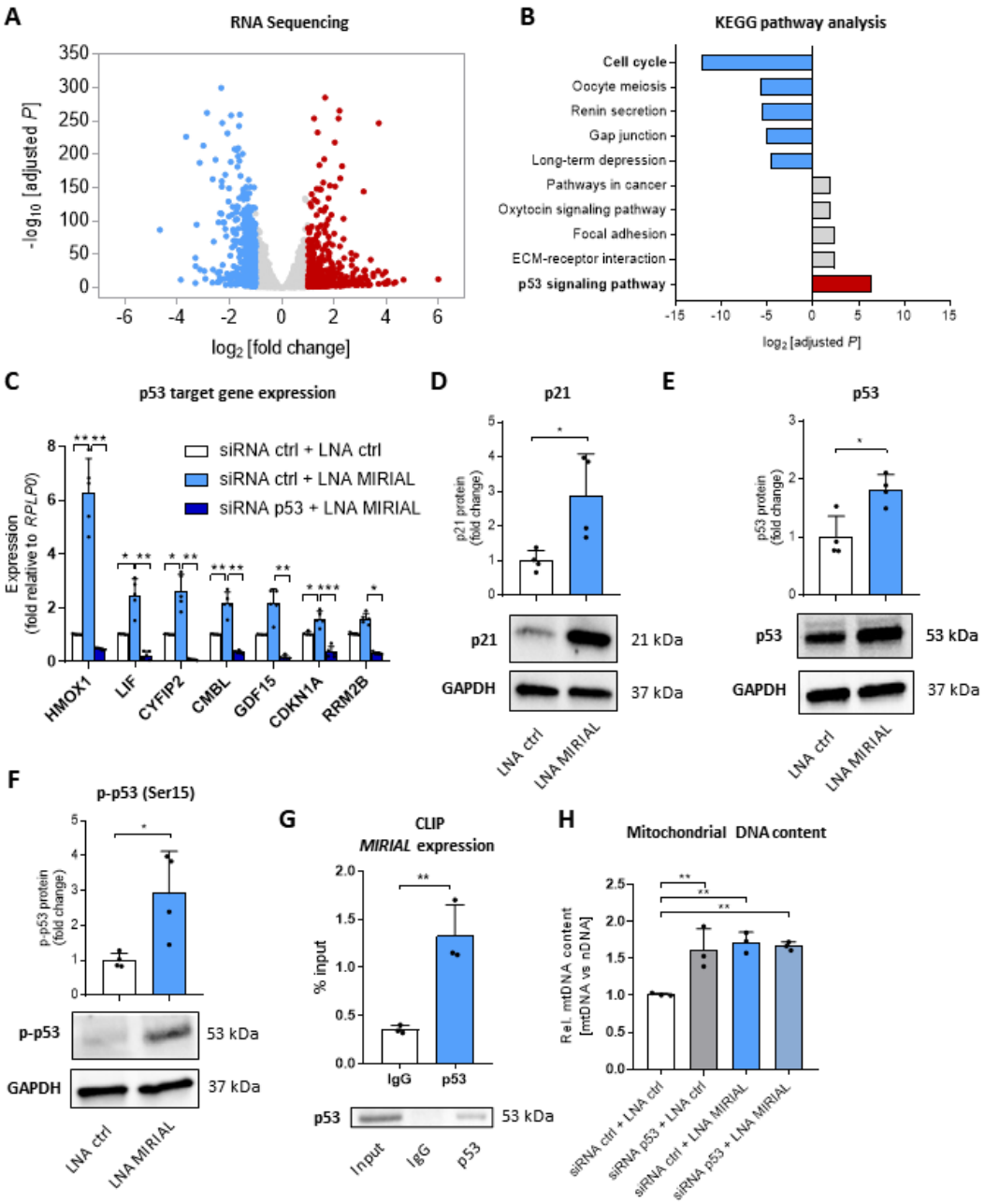

743

744 **Fig. 3: *MIRIAL* knockdown in HUVECs activates the p53 signaling pathway**

745 **A** Volcano plot representing differentially expressed genes from RNA-sequencing of HUVECs

746 48h after transfection with either gapmeRs targeting *MIRIAL* (20 nM) or control gapmeRs

747 (control vs *MIRIAL* knockdown; colored dots fold change≥2; adj. p≤0.01.; n=4). **B** KEGG

748 pathway analysis of RNA-sequencing data in fig. 3A. **C** p53 target gene expression in HUVECs

749 48h after gapmeR-mediated *MIRIAL* knockdown (20 nM) compared to control-transfected
750 HUVECs and siRNA-mediated knockdown of p53 (10 nM) or control transfected HUVECs,
751 using qRT-PCR (n=5; Brown-Forsythe and Welch ANOVA). **D** Protein levels of p21 in HUVECs
752 48h after gapmeR-mediated *MIRIAL* knockdown (20 nM) compared to control-transfected
753 HUVECs using Western Blot (n=4; unpaired t test). **E** Protein levels of p53 in HUVECs 48h
754 after gapmeR-mediated *MIRIAL* knockdown (20 nM) compared to control-transfected
755 HUVECs using Western Blot (n=4; unpaired t test). **F** Protein levels of phosphorylated p53
756 (Ser15) in HUVECs 48h after gapmeR-mediated *MIRIAL* knockdown (20 nM) compared to
757 control-transfected HUVECs using Western Blot (n=4; unpaired t test). **G** *MIRIAL* expression
758 measured by qRT-PCR after crosslinking and RNA immunoprecipitation (CLIP) of HUVEC
759 lysate with a p53 antibody or IgG isotype control antibody (5 µg each) and Western blot
760 analysis of p53 in the input and immunoprecipitates (n=3; unpaired t test). **H** Mitochondrial
761 DNA (mtDNA) content relative to nuclear DNA (nDNA) content of HUVECs 48h after gapmeR-
762 mediated *MIRIAL* knockdown (20 nM) compared to control-transfected HUVECs and siRNA-
763 mediated knockdown of p53 (10 nM) or control transfected HUVECs using qPCR (n=3;
764 ANOVA). Results are expressed as mean ± s.d.; *p<0.05, **p<0.01, ***p<0.001

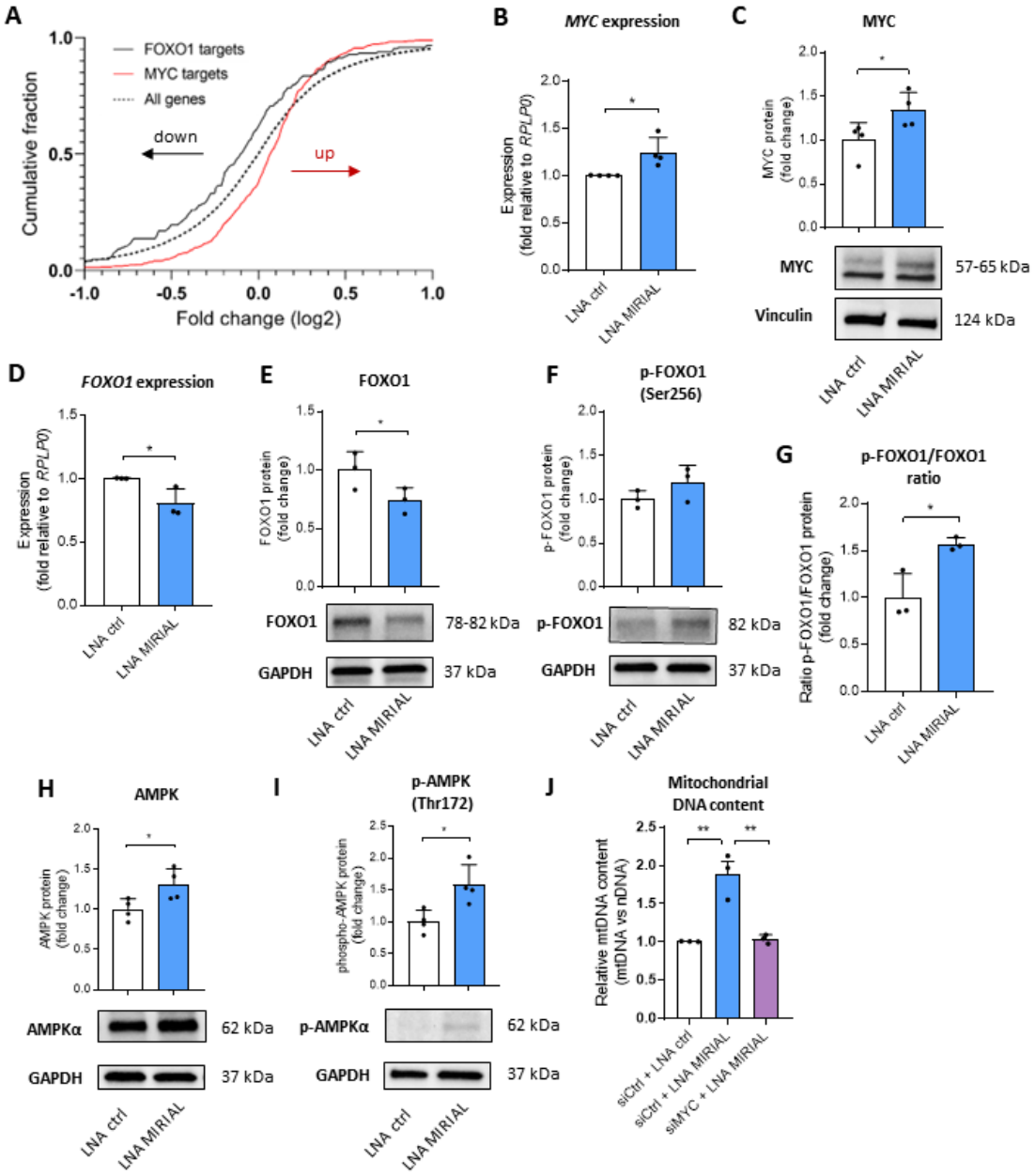

Fig. 4: *MIRIAL* regulates endothelial quiescence through FOXO1 and MYC

A Expression changes of MYC nuclear target genes encoding mitochondrial proteins and FOXO1 target genes compared to all genes 48h after gapmeR-mediated *MIRIAL* knockdown (20 nM) in HUVECs compared to control-transfected HUVECs using RNAseq (*n*=4). **B** *MYC* expression in HUVECs 48h after gapmeR-mediated *MIRIAL* knockdown (20 nM) compared to control-transfected HUVECs using qPCR (*n*=4; Mann-Whitney test). **C** Protein levels of MYC in

772 HUVECs 48h after gapmeR-mediated *MIRIAL* knockdown (20 nM) compared to control-
773 transfected HUVECs using Western blot (*n*=4; Mann-Whitney test). **D** *FOXO1* expression in
774 HUVECs 48h after gapmeR-mediated *MIRIAL* knockdown (20 nM) compared to control-
775 transfected HUVECs using qRT-PCR (*n*=3; unpaired *t* test). **E** Protein levels of FOXO1 in
776 HUVECs 48h after gapmeR-mediated *MIRIAL* knockdown (20 nM) compared to control-
777 transfected HUVECs using Western blot (*n*=3; paired *t* test). **F** Protein levels of
778 phosphorylated FOXO1 (Ser256) in HUVECs 48h after gapmeR-mediated *MIRIAL* knockdown
779 (20 nM) compared to control-transfected HUVECs using Western blot (*n*=3; paired *t* test). **G**
780 Ratio of phosphorylated to total protein levels of FOXO1 in HUVECs 48h after gapmeR-
781 mediated *MIRIAL* knockdown (20 nM) compared to control-transfected HUVECs quantified
782 from fig. 4 E and F (*n*=3; unpaired *t* test). **H** Protein levels of AMPK in HUVECs 48h after
783 gapmeR-mediated *MIRIAL* knockdown (20 nM) compared to control-transfected HUVECs
784 using Western blot (*n*=4; unpaired *t* test). **I** Protein levels of phosphorylated AMPK (Thr172)
785 in HUVECs 48h after gapmeR-mediated *MIRIAL* knockdown (20 nM) compared to control-
786 transfected HUVECs using Western blot (*n*=4; unpaired *t* test). **J** Mitochondrial DNA (mtDNA)
787 content relative to nuclear DNA (nDNA) content of HUVECs 48h after gapmeR-mediated
788 *MIRIAL* knockdown (20 nM) compared to control-transfected HUVECs and siRNA-mediated
789 knockdown of MYC (60 nM) or control transfected HUVECs using qPCR (*n*=3; ANOVA).
790 Results are expressed as mean ± s.d.; *$p<0.05$, **$p<0.01$

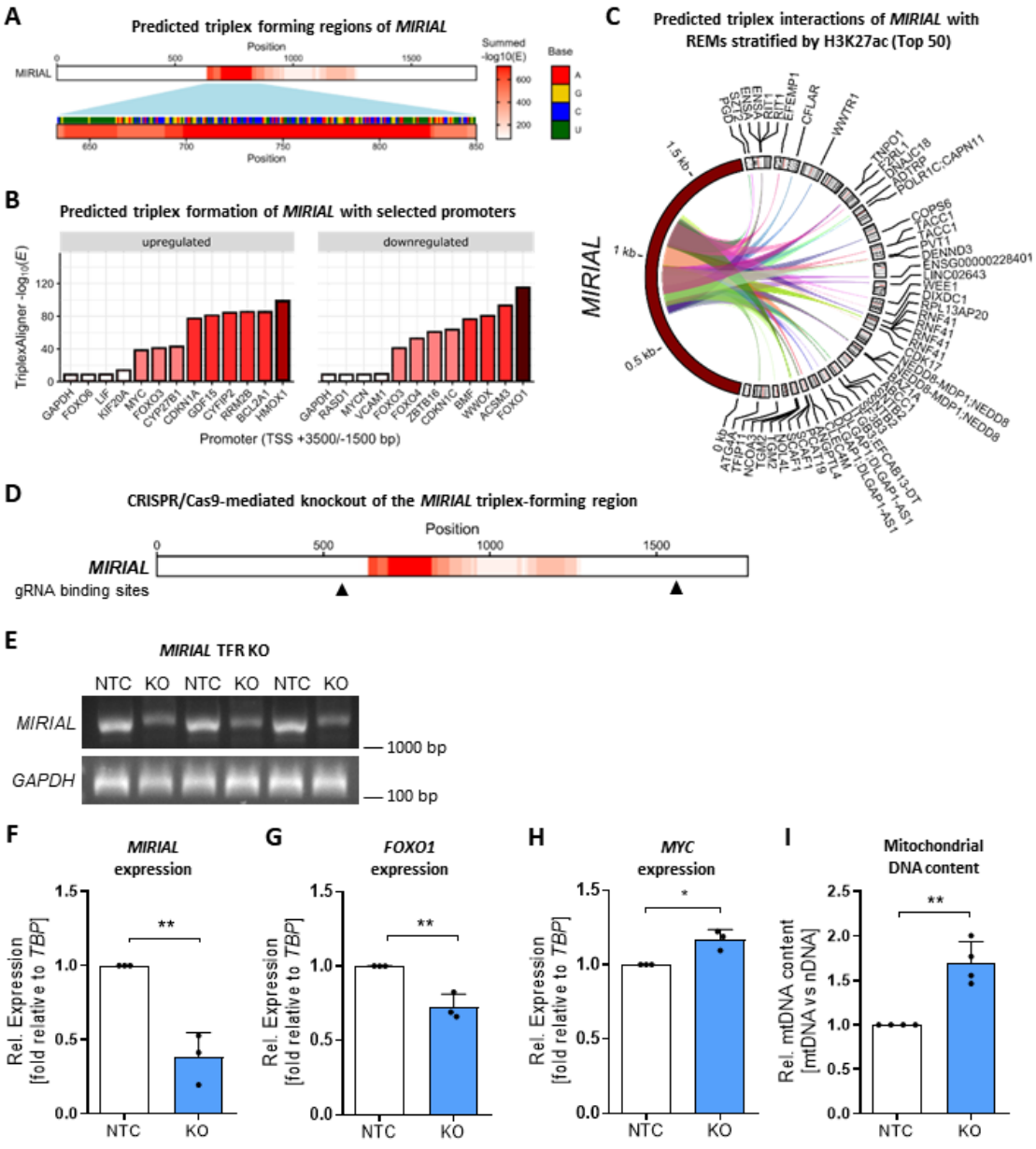

Fig. 5: *MIRIAL* forms *RNA*·DNA:DNA triplexes in the *FOXO1* promoter region

A Schematic representation of the lncRNA *MIRIAL* showing predicted probability (-log10(E) values) of *RNA*·DNA:DNA triplex forming regions (TFRs) in the lncRNA using *TriplexAligner*. **B** *TriplexAligner* scores (-log10(E) values) for predicted interactions between the lncRNA *MIRIAL* and selected promoters of genes upregulated after *MIRIAL* knockdown (*FOXO6, LIF, KIF20A, MYC, CYP27B1, CDKN1A, GDF15, CYFIP2, RRM2B, BCL2A1, HMOX1*) or

798 downregulated after *MIRIAL* knockdown (*RASD1, MYCN, VCAM1, FOXO4, ZBTB16, CDKN1C,*
799 *BMF, WWOX, ACSM3, FOXO1*) in RNAseq (fig. 3A), in comparison to negative control
800 promoters of genes that are not regulated after *MIRIAL* knockdown (*GAPDH* and *FOXO3*)
801 using *TriplexAligner*. **C** Top 50 predicted triplex interactions of *MIRIAL* with regulatory
802 elements (REMs) using *TriplexAligner* ranked by *TriplexAligner* score and stratified by
803 genome accessibility (H3K27ac) data obtained from ENCODE. **D** Schematic representation of
804 the *MIRIAL* transcript and the binding sites of guide RNAs (gRNAs) used for CRISPR/Cas9-
805 mediated knockout (KO) of the triplex-forming region (TFR) of *MIRIAL*. **E** CRISPR/Cas9-
806 mediated knockout (KO) of the *MIRIAL* TFR in HUVECs using lentiviral transduction of
807 *MIRIAL*-targeting guide-RNAs or non-targeting control (NTC) gRNAs and measured my
808 genomic DNA PCR 10 days post-transduction. *GAPDH* serves as loading control. Three
809 independent experiments are shown. **F** *MIRIAL* expression after CRISPR/Cas9-mediated
810 knockout (KO) of the *MIRIAL* TFR or non-targeting control (NTC) using qRT-PCR (n=3;
811 unpaired t test). **G** *FOXO1* expression in HUVECs 10 days after CRISPR/Cas9-mediated *MIRIAL*
812 TFR knockout compared to control-transduced HUVECs using qRT-PCR (n=3; unpaired t test).
813 **H** *MYC* expression in HUVECs 10 days after CRISPR/Cas9-mediated *MIRIAL* TFR knockout
814 compared to control-transduced HUVECs using qRT-PCR (n=3; unpaired t test). **I**
815 Mitochondrial DNA (mtDNA) content relative to nuclear DNA (nDNA) content of HUVECs 10
816 days after CRISPR/Cas9-mediated *MIRIAL* TFR knockout compared to control-transduced
817 HUVECs using qPCR (n=4; unpaired t test). Results are expressed as mean ± s.d.; *p<0.05,
818 **p<0.01

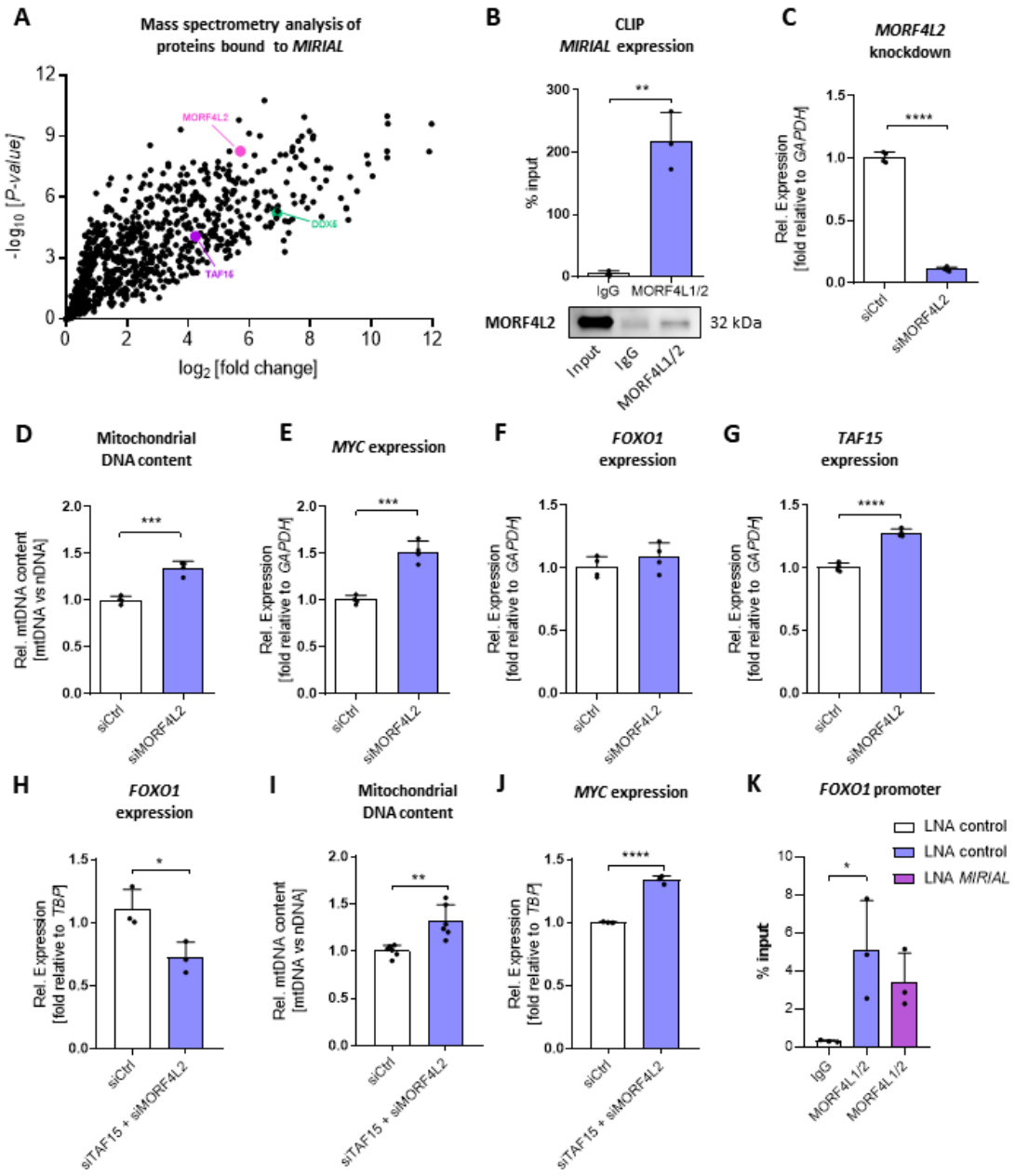

Fig. 6: *MIRIAL* recruits Mortality Factor 4 Like 2 (MORF4L2) and TATA-binding Protein-associated Factor 2N (TAF15) to the *FOXO1* transcriptional start site

A Volcano plot depicting all proteins from nuclear lysates enriched in *MIRIAL* pulldown as compared to pulldown with a scrambled oligo, identified by mass spectrometry (*n*=6; unpaired *t* test). **B** *MIRIAL* expression measured by qRT-PCR after crosslinking and RNA immunoprecipitation (CLIP) of HUVEC lysate with a MORF4L1/2 antibody or IgG isotype

826 control antibody (5 µg each) and Western blot analysis of MORF4L2 in the input and
827 immunoprecipitates (*n*=3; unpaired *t* test). **C** *MORF4L2* expression in HUVECs 48h after
828 siRNA-mediated *MORF4L2* knockdown (10 nM) compared to control-transfected HUVECs
829 using qRT-PCR (*n*=4; unpaired *t* test). **D** Mitochondrial DNA (mtDNA) content relative to
830 nuclear DNA (nDNA) content in HUVECs 48h after siRNA-mediated *MORF4L2* knockdown (10
831 nM) compared to control-transfected HUVECs using qPCR (*n*=4; unpaired *t* test). **E** *MYC*
832 expression in HUVECs 48h after siRNA-mediated *MORF4L2* knockdown (10 nM) compared to
833 control-transfected HUVECs using qRT-PCR (*n*=4; unpaired *t* test). **F** *FOXO1* expression in
834 HUVECs 48h after siRNA-mediated *MORF4L2* knockdown (10 nM) compared to control-
835 transfected HUVECs using qRT-PCR (*n*=4; unpaired *t* test). **G** *TAF15* expression in HUVECs 48h
836 after siRNA-mediated *MORF4L2* knockdown (10 nM) compared to control-transfected
837 HUVECs using qRT-PCR (*n*=4; unpaired *t* test). **H** *FOXO1* expression in HUVECs 48h after
838 siRNA-mediated knockdown of *MORF4L2* and *TAF15* (10 nM each) compared to control-
839 transfected HUVECs using qRT-PCR (*n*=3; unpaired *t* test). **I** Mitochondrial DNA (mtDNA)
840 content relative to nuclear DNA (nDNA) content in HUVECs 48h after siRNA-mediated
841 knockdown of *MORF4L2* and *TAF15* (10 nM each) compared to control-transfected HUVECs
842 using qPCR (*n*=6; unpaired *t* test). **J** *MYC* expression in HUVECs 48h after siRNA-mediated
843 knockdown of *MORF4L2* and *TAF15* (10 nM each) compared to control-transfected HUVECs
844 using qRT-PCR (*n*=3; unpaired *t* test). **K** *FOXO1* promoter sequence measured by qPCR in
845 HUVEC nuclear lysates after chromatin immunoprecipitation (ChIP) using a MORF4L1/2
846 antibody (5 µg) or IgG isotype control antibody (1 µg). ChIP was performed 48 h after
847 gapmeR-mediated knockdown of *MIRIAL* (20 nM) and compared to control-transfected
848 HUVECs (*n*=3; ANOVA). Results are expressed as mean ± s.d.; **p*<0.05, ***p*<0.01,
849 ****p*<0.001, *****p*<0.0001

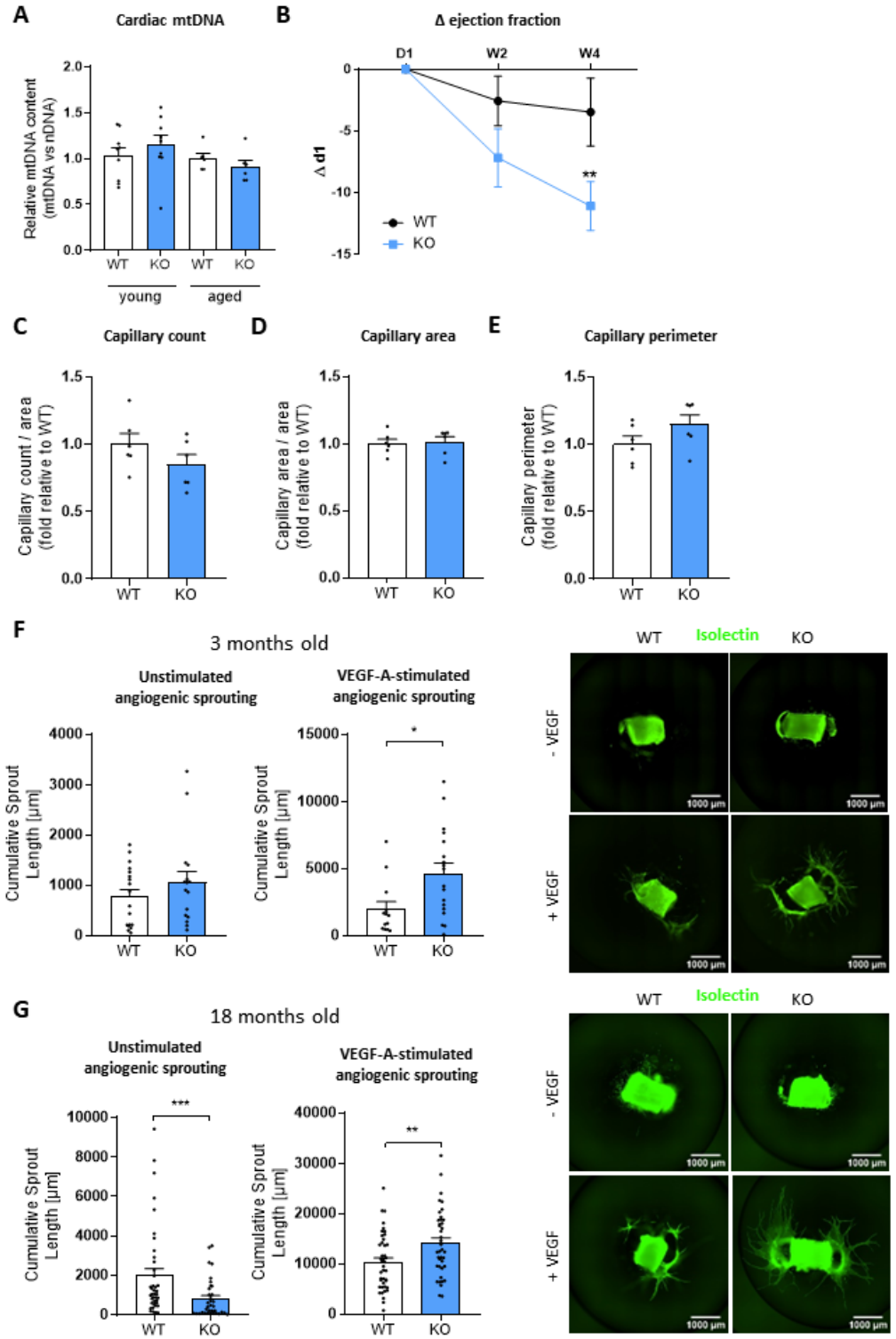

850

851 **Fig. 7: *Mirial* KO in mice decreases EF after acute myocardial infarction and regulates**

852 **angiogenic sprouting *ex vivo***

853 **A** Mitochondrial DNA (mtDNA) content relative to nuclear DNA (nDNA) content in heart
854 tissue of young (3 months) and aged (18 months) *Mirial* KO mice and their WT littermates
855 using qPCR (*n*=9 and 6 mice per group; ANOVA). **B** Cardiac contractile function of *Mirial* KO
856 mice and their wildtype (WT) littermates assessed by echocardiography displayed as delta
857 ejection fraction values two weeks (W2) or four weeks (W4) after AMI in comparison to day
858 1 (D1) (*n*=6; ANOVA). **C** Capillary count in serial cardiac sections of the infarct border zone 4
859 weeks after AMI surgery of *Mirial* KO mice (11-13 weeks) and their wildtype (WT)
860 littermates. ECs were stained using Isolectin B4 and analyzed using confocal microscopy.
861 Representative images are shown in supp. fig. 8E. Per mouse, three sections were analyzed
862 (*n*=6; unpaired *t* test). **D** Capillary area in serial cardiac sections of the infarct border zone 4
863 weeks after AMI surgery of *Mirial* KO mice (11-13 weeks) and their wildtype (WT)
864 littermates. ECs were stained using Isolectin B4 and analyzed using confocal microscopy.
865 Representative images are shown in supp. fig. 8E. Per mouse, three sections were analyzed
866 (*n*=6; Mann-Whitney test). **E** Capillary perimeter in serial cardiac sections of the infarct
867 border zone 4 weeks after AMI surgery of *Mirial* KO mice (11-13 weeks) and their wildtype
868 (WT) littermates. ECs were stained using Isolectin B4 and analyzed using confocal
869 microscopy. Representative images are shown in supp. fig. 8E. Per mouse, three sections
870 were analyzed (*n*=6; unpaired *t* test). **F** Cumulative sprout length from aortic rings of young
871 (3 months) *Mirial* KO mice and WT littermates under basal and VEGF-stimulated (30 ng/mL)
872 conditions (*n*=6 mice per group; Mann-Whitney test). ECs were stained with Isolectin B4 and
873 analyzed using immunofluorescence microscopy. 2-8 aortic rings per mouse were analyzed.
874 **G** Cumulative sprout length from aortic rings of aged (18 months) *Mirial* KO mice and WT
875 littermates under basal and VEGF-stimulated (30 ng/mL) conditions (*n*=6 mice per group;
876 Mann-Whitney test and unpaired *t* test). ECs were stained with Isolectin B4 and analyzed

877 using immunofluorescence microscopy. 5-8 aortic rings per mouse were analyzed. Results

878 are expressed as mean ± s.e.m.; *p<0.05, **p<0.01, ***p<0.001